


***Ab initio* insights on the fermiology of d^1 transition metals on the honeycomb lattice: Hierarchy of hopping pathways and spin-orbit coupling**

Manoj Gupta ^{1,*}, Basudeb Mondal^{2,*}, Subhro Bhattacharjee ^{2,*} and Tanusri Saha Dasgupta ^{1,||}

¹*Department of Condensed Matter Physics and Materials Science, S. N. Bose National Centre for Basic Sciences, Kolkata 700098, India*

²*International Centre for Theoretical Sciences, Tata Institute of Fundamental Research, Bengaluru 560 089, India*

 (Received 14 August 2023; revised 28 September 2023; accepted 1 November 2023; published 8 December 2023)

Recently, the physics of $J = 3/2$ electrons on a honeycomb lattice has received attention with the suggestion of hosting an SU(8) Dirac semimetallic state. Motivated by this, in this work we provide a systematic study of the interplay of various hopping pathways and atomic spin-orbit coupling for the low-energy electrons in candidate d^1 transition-metal halides MX_3 ($M = \text{Ti, Zr, Hf}$; $X = \text{F, Cl, Br}$). By combining first-principles calculations and a minimal hopping Hamiltonian, we uncover the role of dominant direct metal-metal hopping on top of indirect metal-halide-metal hopping. This sets up a hierarchy of hopping pathways that centrally modify the SU(8) picture for the above materials. These hopping interactions, along with the spin-orbit coupling, lead to a plethora of exactly compensated metals instead of the SU(8) Dirac semimetal. Remarkably, the same can be understood as descendants of a topological insulator obtained by gapping out the SU(8) Dirac semimetallic phase. The resultant compensated metals have varied Fermi surface topology and are separated by Lifshitz phase transitions. We discuss the implications of the proximate Lifshitz transition, which may be accessed via strain, in the context of the relevant materials.

DOI: [10.1103/PhysRevResearch.5.043219](https://doi.org/10.1103/PhysRevResearch.5.043219)

I. INTRODUCTION

Electronic phases of transition-metal compounds with active d electrons pose some of the outstanding problems in condensed matter physics. In addition to the well-known effect of electron-electron interactions, in recent times it has been realized that atomic spin-orbit coupling (SOC) plays an important role in shaping the structure of the low-energy theory of the $4d$ and $5d$ transition-metal compounds [1,2]. This provides the scope to study, design, and engineer newer platforms of quantum materials supporting novel electronic phases resulting from the interplay of quantum entanglement and symmetries as evidenced in spin-orbit-assisted Mott insulators, quantum spin liquids, excitonic magnetism, multipolar orderings, and correlated topological semimetals [3–13].

In particular, for $4d$ and $5d$ transition metals in an octahedral crystal field and with active t_{2g} orbitals, the strong SOC can split the atomic t_{2g} orbitals into an effective higher-energy $J = 1/2$ doublet and a lower-energy $J = 3/2$ quadruplet [3]. In this regard, the physics of the $J = 1/2$ orbitals has been

studied extensively [14–16]. In comparison, the compounds with active $J = 3/2$ manifold have received somewhat less attention in spite of the potential to harbor equally or even richer low-energy physics.

Potential candidates of expected $J = 3/2$ physics are the transition-metal compounds in the d^1 electronic state where the t_{2g} orbitals are at $1/6$ filling. At the strong-SOC limit, this leads to an empty $J = 1/2$ manifold, while the $J = 3/2$ orbitals are quarter filled. Among these compounds, of particular interest to us are layered transition-metal (M) halides (X), of the general formula MX_3 [17]. The 3^+ transition-metal (M) cations in these compounds, in the octahedral setting of 1^{-1} halide anions, form a honeycomb lattice by edge sharing of MX_6 octahedra. Yamada *et al.* [18] proposed ZrCl_3 , a member of the honeycomb d^1 family, as a candidate material exhibiting an SU(4) symmetric spin Hamiltonian in the strong-coupling limit. Mondal *et al.* [19] showed that the same can lead to an SU(8) Dirac semimetal (DSM) in the noninteracting electron limit.

It is to be noted, though, that the above Hamiltonian(s) were derived under the assumption of an infinite SOC limit by projecting to the $J = 3/2$ orbitals, and by considering only indirect hopping, i.e., hopping between two M sites via the X . As expected, both of these assumptions are idealized limits vis-à-vis the candidate materials. There are other microscopic energy scales even at the single-electron level—the various hopping amplitudes and noncubic crystal field splitting—that can compete and change the low-energy physics, and hence need to be understood. While the SU(4) or SU(8) may provide an interesting starting point to capture the strong- and intermediate-coupling physics in real materials, generally one expects that these other energy scales would reduce the

*These authors contributed equally to this work.

†gpta.mnj@gmail.com

‡basudeb.mondal@icts.res.in

§subhro@icts.res.in

||t.sahadasgupta@gmail.com

Published by the American Physical Society under the terms of the Creative Commons Attribution 4.0 International license. Further distribution of this work must maintain attribution to the author(s) and the published article's title, journal citation, and DOI.

fine-tuned symmetries for the spin model or the free Dirac theory, respectively. What then are the resultant structure of the low-energy theory and the possible electronic phases in this family of materials? More interestingly, the details of these competing microscopic interactions can change across the periodic table even within the same class of MX_3 materials, e.g., in moving from $3d$ to $4d$ to $5d$ transition metals ($M = \text{Ti} \rightarrow \text{Zr} \rightarrow \text{Hf}$) and in moving from $2p$ to $3p$ to $4p$ halogens ($X = \text{F} \rightarrow \text{Cl} \rightarrow \text{Br}$).

In this paper, we present *ab initio* density functional theory (DFT) insights into the estimates of the different hopping pathways and their effect on the low-energy minimal hopping models to reveal a rich structure of the possible phases relevant to MX_3 . Guided by our DFT calculations, we conclude that the low-energy fermiology of the electrons requires SOC and a minimal set of four hopping pathways that include two direct dd hopping, $t_{dd\sigma}$ and $t_{dd\pi}$, in addition to two well-known [20] indirect ones via the intermediate halide ion, t_{ddm} , $t_{ddm'}$. Across the transition-metal series, the hierarchy of direct and indirect hopping shows an interesting evolution, with the fluorides being notably different from the chlorides and bromides. This results in a marked deviation from the indirect-hopping-only model at large SOC.

Reference [19] showed that an indirect hopping model for the $J = 3/2$ electrons leads to a pair of linear bands touching, i.e., Dirac points, for fourfold-degenerate orbitals arising from a nonmanifest $SU(4)$ symmetry [18]. The $SU(4)$ symmetry, combined with the valley, gives rise to a spin-orbit-coupled $SU(8)$ DSM [19], which, we show here, provides a controlled understanding of the effect of the other hopping pathways as well as finite SOC. Our DFT results suggest that the largest of the microscopic energy scales is the direct overlap between the transition-metal ions, $t_{dd\sigma}$. This, along with finite SOC (λ), allowing for the mixing among the different t_{2g} orbitals, provides a natural setting to explore the phase diagram in the $(t_{dd\sigma}/t_{ddm})$ - λ plane around the $SU(8)$ semimetal. For chlorides and bromides, the effect of both these perturbations can be understood in terms of gapping out of the $SU(8)$ Dirac fermions. However, while finite $t_{dd\sigma}$ gives a Z_2 free fermion symmetry-protected topological (SPT) insulator [21,22], finite λ leads to a trivial one with an intervening $SU(2)$ DSM line separating the two. The primary effect of subleading direct and indirect hopping, $t_{dd\pi}$ and $t_{ddm'}$, is to change the details of the band structure around the Fermi level to give rise to particle-hole pockets resulting in a plethora of exactly compensated metals with varied Fermi surface topology. Two characteristic features of the Fermi surfaces relevant for the materials, we note, are (a) near nesting of different sections of the Fermi pockets, and (b) proximity to Lifshitz transition which leads to the change in the Fermi surface topology. Remarkably, all these compensated metals are direct descendants of the topological insulator obtained in the $SU(8)$ limit and carry a nontrivial Z_2 index. Using our *ab initio* estimates of the band parameters, we place various materials (chlorides and bromides) on the relevant part of the λ -hopping phase diagram. Interestingly, we find that the chlorides lie close to the phase boundary between the different compensated metals separated by a Lifshitz transition. This opens up the possibility of strain-induced Lifshitz transition in monolayer MCl_3 .

The rest of the paper is organized as follows. In Sec. II we introduce the DFT computation details that we use to obtain the electronic band structure, as well as the construction of the low-energy Hamiltonian of the compounds. In Sec. III, the crystal structure of the nine compounds, MX_3 where $M = \text{Ti}, \text{Zr}, \text{Hf}$ and $X = \text{F}, \text{Cl}, \text{Br}$, is discussed. This is followed by the discussion of DFT band structure in Sec. IV and the DFT-derived low-energy tight-binding model in Sec. V. The phase diagrams of the low-energy hopping model in SOC strength and hopping space upon systematic introduction of hopping are discussed in subsequent sections (cfs Sec. VI). This also includes the phase diagram relevant to the discussed chloride and bromide compounds and discussion of the possible Lifshitz transition. We close the result section with a brief overview on the consequences of parameters relevant for fluorides in the $(t_{dd\sigma}/t_{ddm})$ - λ phase diagram in Sec. VII. In Sec. VIII, a summary and outlook are presented. Supporting technical details are given in the Appendixes.

II. METHODS AND COMPUTATIONAL DETAILS

The first-principles DFT calculations were carried out using a plane-wave basis and projector augmented-wave potential [23–25], as implemented in the Vienna Ab initio Simulation package [26–28]. The Perdew-Burke-Ernzerhof generalized gradient approximation (GGA) [29] was used to approximate the exchange-correlation functional. To check the influence of the correlation effect at the transition-metal site, beyond GGA, GGA + U with supplemented Hubbard U correction was carried out [30]. Furthermore, to handle the van der Waals interaction between the layers, a dispersion-corrected GGA + U + D2 functional was used [31]. The convergence of energies and forces was ensured by using a plane-wave energy cutoff of 600 eV and Brillouin zone (BZ) sampling with $6 \times 6 \times 6$ Monkhorst-Pack grids. During the structural relaxation, the ions were allowed to move until the atomic forces became lower than 0.0001 eV/Å.

The construction of a DFT-derived low-energy, few-band Hamiltonian in the effective t_{2g} Wannier basis of the transition-metal ions was achieved through the downfolding technique of integrating out degrees of freedom that are not of interest, starting from the all-orbital DFT band structure, calculated in the muffin-tin orbital (MTO) basis. The self-consistent potentials required for these calculations were generated through the Stuttgart implementation of the linear MTO (LMTO) package [32], while the downfolding calculations were performed in N th-order MTO (NMTO) basis [33]. For muffin-tin orbital calculations, the metal-atom-centered (MT) radii were chosen to be in the ranges 1.30–1.53 Å, 1.47–1.66 Å, and 1.44–1.70 Å for Ti, Zr, and Hf, respectively. The MT radii of 0.94–0.97 Å, 1.33–1.34 Å, and 1.46–1.48 Å were chosen for halogen atoms F, Cl, and Br, respectively. The consistency of the results between plane-wave and muffin-tin orbital basis was checked in terms of band structure and density of states.

The phases for the effective tight-binding models are obtained following standard numerical procedures by solving for the band structure for different values of the parameters, subject to the 1/6 filling. The details are summarized in Appendix A.

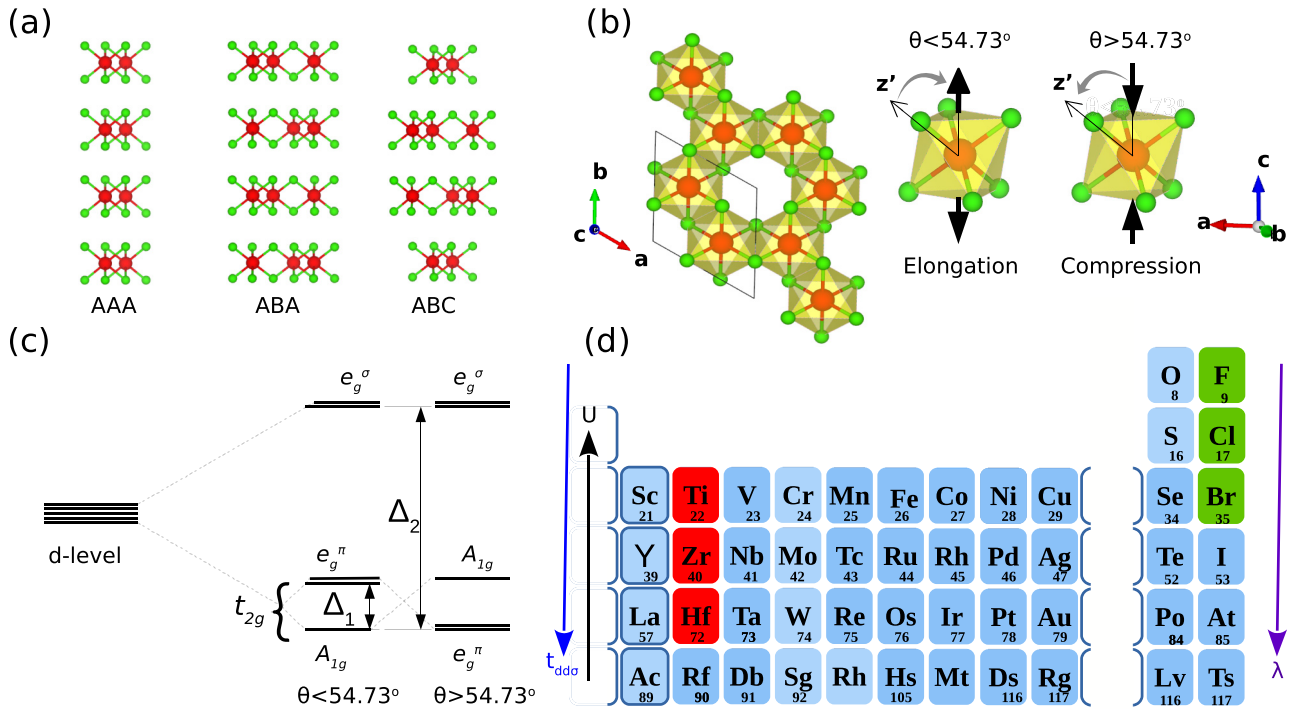


FIG. 1. (a) Different possible stacking of the honeycomb layers in MX_3 family. The M and X atoms are shown as red and green balls, respectively. (b) Left: The honeycomb layer of M atoms formed by the edge-sharing of MX_6 octahedra. Right: The trigonal distortion of the MX_6 octahedra. (c) The octahedral (Δ_2) and trigonal (Δ_1) crystal field splitting of the d levels of M . (d) The choice of M (marked in red) and X (marked in green) elements of the compounds under study. The variation of the three primary energy scales of the problem: SOC (λ), orbital size dictating the direct metal-metal hopping ($t_{dd\sigma}$), and Coulomb interaction (U).

III. CRYSTAL STRUCTURE AND d -LEVEL SPLITTING OF THE STUDIED COMPOUNDS

The layered structure of MX_3 compounds comprises two-dimensional hexagonal nets of MX_3 , van der Waals stacked on each other. Clearly, there can be many variants of the stacking sequence in these layered materials. Due to the weak van der Waals interactions between layers, different stacking sequences result only in small energy differences. For example, $TiCl_3$ is reported to adopt ABA, AAA, and ABC stacking sequences, as shown in Fig. 1(a), with ABA stacking resulting in $P\bar{3}1c$ [34], AAA stacking in $P\bar{3}1m$ [35], and ABC stacking in $R\bar{3}$ [34] space groups. Though these polymorphs have different crystal space groups, their in-plane geometry as well as interlayer distance show little variation, less than 0.2% for the specific case of $TiCl_3$ [36]. The weak van der Waals interaction of ~ 1 meV between the layers allows the structure to transform from one stacking type to another, depending on the synthesis procedure. Since we are primarily interested in the in-plane physics of the hexagonal net of d^1 transition metals, for simplicity we will assume AAA stacking of the compounds in the rest of the discussion.

As per the available literature [17] on the layered MX_3 compounds, these compounds have been reported to adopt either in the rhombohedral BiI_3 type [37], or the monoclinic $AlCl_3$ structure type [38]. In the BiI_3 structure, the honeycomb net is regular due to the threefold symmetry, with three equal-length metal-metal bonds. In the $AlCl_3$ structure, on the other hand, the honeycomb net can be distorted, and the y coordinate of the M site determines the degree of distortion.

This results in two unique in-plane $M-M$ distances. Most compounds report a temperature-driven transition from uniform rhombohedral BiI_3 type to bond-dimerized monoclinic $AlCl_3$ structure. The available data [34] show this structural transition typically happens around 100–200 K for d^1 transition-metal trihalides. In the discussion in the following, we will focus on the AAA stacked high-temperature structure of a uniform honeycomb net of transition metals possessing C_3 symmetry, which would host different possible electronic instabilities. As discussed later, subtle structures in the electron band structure pave the way to electronically driven charge-density-wave instabilities including dimerization, to which the lattice may react.

Although the considered structures hold a uniform hexagonal network of metal atoms, the underlying rhombohedral symmetry allows for the trigonal distortion of the MX_6 octahedra, which occurs as the elongation or compression along one of the four threefold-symmetry axes, as shown in Fig. 1(b). The elongation (compression) results in a decrease (an increase) of the angle (θ) between the $M-X$ bond and the threefold axis from an ideal value of 54.73° . Figure 1(b) shows the crystal splitting of the d levels of M atoms. In the presence of the octahedral splitting, the fivefold-degenerate d levels split into threefold-degenerate t_{2g} and twofold-degenerate e_g^σ . In the presence of trigonal distortion of the MX_6 octahedra, the t_{2g} levels further split into singly degenerate a_{1g} and doubly degenerate e_g^π , with Δ_2 and Δ_1 denoting the octahedral and trigonal splitting, respectively.

As mentioned above, in the present study we focus on the nine d^1 MX_3 compounds with $M = Ti, Zr, Hf$ and $X = F, Cl,$

TABLE I. In-plane lattice constants ($a = b$) and trigonal distortion ($\Delta\theta_{\text{trig}}$) of the theoretically optimized structures of MX_3 . Given also is the information on experimentally synthesized compounds.

	TiX ₃			ZrX ₃			HfX ₃		
	F	Cl	Br	F	Cl	Br	F	Cl	Br
$a = b$ (Å)	5.202	6.030	6.405	5.487	6.204	6.524	5.320	6.096	6.423
$\Delta\theta_{\text{trig}}$ (deg)	2.078	-0.550	-0.714	1.568	-1.133	-1.563	0.815	-1.244	-1.563
Expt. synthesis	No	Yes [35]	Yes ^a [39]	No	Yes ^b [40]	No	No	No	No

^aStructure with space group 148 (ABC stacking) is available.

^bBased on misaligned powder x-ray data.

Br, drawn from $3d$, $4d$, and $5d$ transition-metal series and $2p$, $3p$, and $4p$ series, as shown in Fig. 1(d). The choice of these compounds allows one to study the interplay of SOC and hopping, as well as Coulomb interaction. Moving down the column, the SOC increases due to increase in atomic number, and the metal-metal hopping increases due to an increase in the spatial extent of the d orbitals. Out of the nine proposed compounds, only three compounds, namely, TiCl₃ [34,35,35], TiBr₃ [39], and ZrCl₃ [40], have been experimentally synthesized. To predict the crystal structure of the remaining compounds, we use the available experimental structure of the related compound with either common M or common X as the template and accordingly substitute the metal or the halide atom with the desired element. The constructed structure is subsequently fully relaxed by relaxing the atomic coordinates and the volume, fixing the symmetry. The influence of exchange-correlation and van der Waals interactions were checked in terms calculations within GGA, GGA + U and GGA + U + D2. Among these, the GGA calculation consistently was found to reproduce well the experimentally measured in-plane lattice constants for compounds that have been synthesized. Since we are primarily interested in in-plane physics, in subsequent analysis we consider GGA optimized crystal structures in the $P\bar{3}1m$ space group. The optimized values of in-plane lattice parameters as well as trigonal distortion ($\Delta\theta_{\text{trig}}$) are given in Table I. The in-plane lattice shows an expansion in moving from $2p$ to $3p$ to $4p$, and from $3d$ to $4d$ to $5d$. Interestingly, we note the trigonal distortion in fluoride compounds is opposite that in chloride and bromide.

IV. DFT BAND STRUCTURE

The GGA density of states of the representative compound ZrCl₃, over a broad energy scale of -7 eV below the Fermi level (E_F) and 4 eV above E_F , projected onto Zr d and Cl p states, is shown in Fig. 2(a). We find a large separation between the predominantly X p states (beyond ~ 3.5 eV below E_F) and predominantly M d states (around E_F and above), as expected for early transition-metal halides. The corresponding band structure, plotted along the high-symmetry points of the hexagonal BZ (cf. inset), is shown in Fig. 2(b). As evident from the plot, there are ten spin-degenerate bands arising from the d orbitals of the two M ions in the unit cell that cluster into three groups of three, three, and four spin-degenerate bands. While the highest-energy group of four bands belongs to e_g^σ symmetry, the lower two groups of three bands [cf. Figs. 2(b) and 2(c)], spanning energy ranges of ~ -0.3 to 0.5 eV, and ~ 1 to 0.7 eV, respectively, are of t_{2g} symmetry.

Since the trigonal crystal field splits three t_{2g} 's into $2 + 1$ at each site, this cannot account for the above splitting of the six t_{2g} bands into $3 + 3$. At any rate, the trigonal splitting arising from a distortion of 1° – 2° (cf Table I) is expected to be much smaller compared to the splitting between the two groups, which is about 0.5 eV, as seen in the plot. To resolve this issue, we compute the charge densities corresponding to the $3 + 3$ groups of bands which are shown in Fig. 2(c). As is evident from the charge density plots, the grouping of six t_{2g} bands into $3 + 3$ arises due to a bonding-antibonding combination of t_{2g} orbitals resulting from highly directional, direct overlap of t_{2g} orbitals along the three M - M bonds. The band-structure plots in Fig. 2(c), zoomed onto two t_{2g} manifolds, show also the computed band structure including SOC. As is seen, SOC has a negligible effect on the entire band structure except for lifting degeneracy at the high-symmetry points, Γ , K, and M, which suggests the strength of SOC to be relatively weak, and far from the assumption of an infinite-SOC limit.

The above-discussed broad features of the electronic structure are found in other compounds as well, though they differ in the details. For a comprehensive analysis of the t_{2g} manifold of band structure of all nine MX_3 compounds, see Fig. 3. Moving along the metal series, we find that while Zr and Hf share similar band structure features, that of Ti is different in terms of the individual bandwidths of the bonding and antibonding blocks, as well as in the separation between bonding and antibonding blocks. The similarity of the band-structure features of the Zr and Hf series, and their noticeable difference from the Ti series, arises from lanthanide contraction—the increase in atomic radius is greater between the $3d$ and $4d$ metals than between the $4d$ and $5d$ metals. This contraction translates into strengthening of the direct metal-metal hopping and relative weakening of indirect hopping via the halide ion in Zr and Hf compounds, compared to Ti as is discussed below in detail. While the bonding-antibonding splitting is decided by the direct head-on dd overlap, the individual dispersion of each bonding and antibonding block is given by the lateral dd overlap. With increase in direct dd overlap in Zr and Hf, both head-on and lateral, the bonding-antibonding separation as well as individual widths are enhanced compared to that of Ti compounds. Figure 3 also presents GGA+SOC band structures along with GGA band structures. Comparison of the two establishes the SOC effect to be strongest in Hf, moderate in Zr, and negligible in Ti compounds. Moving along the halogen series, fluoride compounds exhibit markedly different dispersion compared to chloride or bromide counterparts, hinting that electronic properties of fluorides are different from chloride and bromide. A bulk of the discussion,

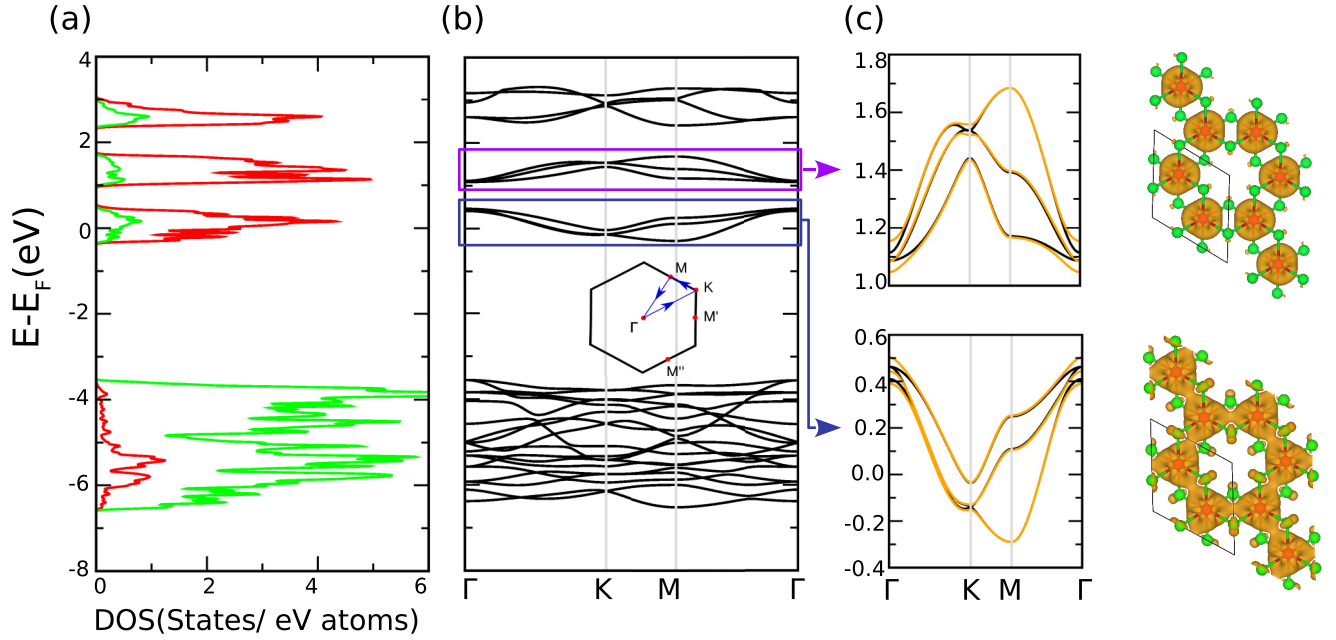


FIG. 2. (a) GGA density of states of ZrCl_3 , projected to Zr d (red) and Cl p (green) states. (b) The corresponding band structure plotted along the high-symmetry points of the hexagonal BZ (shown as inset). (c) Zoomed-in band structure of bonding and antibonding t_{2g} bands and the associated charge densities, with isosurface value chosen to be $0.009 e^-/\text{\AA}^3$. The zoomed-in band-structure plot also includes the comparison of GGA (black) and GGA+SOC (yellow) bands. The zero of the energy in the density of states and band-structure plots are set at corresponding Fermi energy.

therefore, will concentrate on the chlorides and bromides while we summarize briefly the fluorides in Sec. VII.

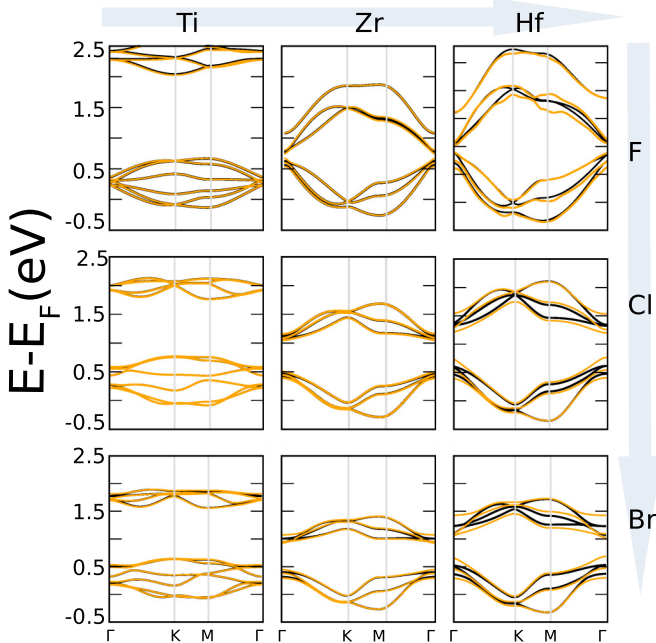


FIG. 3. The variation in band structure of MX_3 (black, GGA; yellow, GGA+SOC), upon change of metal ion from $3d$ Ti \rightarrow $4d$ Zr \rightarrow $5d$ Hf, along the row, and change of halogen from $2p$ F \rightarrow $3p$ Cl \rightarrow $4p$ Br, calculated within GGA. Fermi energy is set to zero in the plots.

V. EFFECTIVE LOW-ENERGY TIGHT-BINDING MODEL

With the above DFT results, we now turn to the low-energy modeling of the above band structure via an effective low-energy tight-binding Hamiltonian for the t_{2g} orbitals in the presence of SOC.

According to molecular orbital theory [41], any two t_{2g} orbitals on adjacent sites can interact to form six levels as σ^* , π^* , δ^* , σ , π , and δ , where we rank them from the highest to the lowest energy. The energy levels σ and σ^* are the consequence of the direct head-on overlap of the d -orbital lobes called $dd\sigma$, whereas direct lateral overlap of d orbitals known as $dd\pi$ and $dd\delta$ gives rise to π^* , δ^* , π , and δ levels, respectively. Among these, δ bonds are weakest and neglected henceforth. These overlaps, along with indirect overlaps via the halide ion, dictate the nature of the resultant tight-binding model in the t_{2g} basis for single-electron kinetic energy, which is the starting point for our low-energy analysis.

In order to provide realistic estimates of these direct and indirect overlap mediated hopping integrals, we derived the low-energy Hamiltonian in the effective transition metal t_{2g} Wannier basis, starting from the full DFT band structure. For this purpose, we constructed the effective Wannier functions by keeping only the metal t_{2g} degrees of freedom in the basis and integrating out the rest through the NMTO downfolding technique. Figure 4(a) shows the comparison of the band structure in the downfolded basis, in comparison to the full band structure. The good comparison justifies the effectiveness of the prescription followed in deriving the low-energy model.

The real-space representation of the downfolded bands shows nonzero hopping amplitudes up to the fourth-nearest

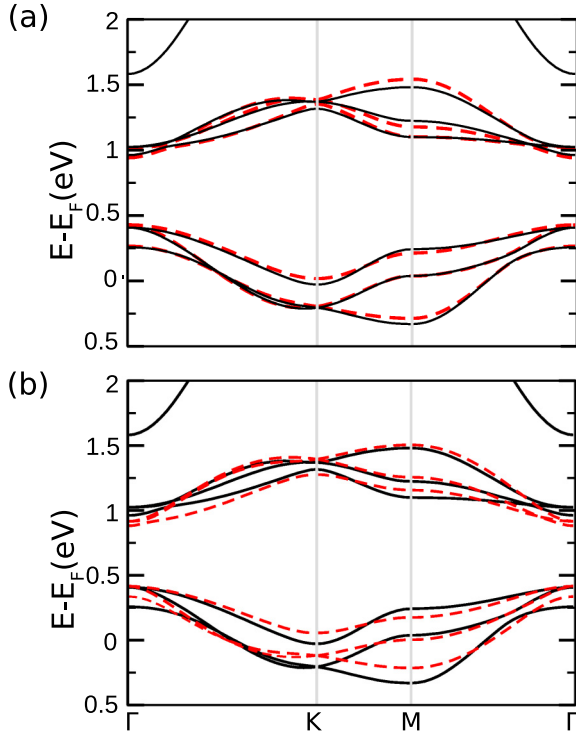


FIG. 4. (a) Downfolded t_{2g} bands (in red) of ZrCl_3 , obtained by integrating all of the degrees of freedom other than Zr t_{2g} in comparison to the DFT band structure (in black). (b) The tight-binding bands (in red), obtained by restricting the real-space representation of the downfolded t_{2g} Hamiltonian to only nearest-neighbor Zr-Zr hopping, in comparison to the DFT band structure (in black). Zero of the energy is set at Fermi energy in (a) and (b).

neighbor (NN) among metal ions. However, a more amenable minimal hopping model with only first-NN interaction is sufficient to reproduce most of the qualitative and quantitative features of the bands, as can be seen in Fig. 4 for ZrCl_3 . A similar conclusion holds also for other materials.

The resultant first-NN tight-binding Hamiltonian in the t_{2g} basis consists of four essential hopping amplitudes: the direct overlap between neighboring t_{2g} orbitals that forms a σ bond denoted by $t_{dd\sigma}$ [cf. Fig. 5(a), left panel, shown for the representative case of ZrCl_3]; the direct overlap between neighboring t_{2g} orbitals that forms a π bond denoted by $t_{dd\pi}$ [cf. Fig. 5(a), right panel, shown for ZrCl_3]; and two indirect overlaps between neighboring t_{2g} orbitals via the halides in the edge-sharing octahedral geometry denoted by t_{ddm} , $t_{ddm'}$, illustrated in Fig. 5(b), for ZrCl_3 . Note that the d orbitals are defined with respect to the local primed halogen-based coordinate system (cf. Fig. 5). For details of transformation between different coordinate systems, see the Appendixes.

Note that in addition to the above hopping parameters, we also have the on-site trigonal energy scale. However, we find that in the presence of the dominant effect of $t_{dd\sigma}$, which is responsible for creating the bonding and antibonding orbitals [cf. Fig. 2(c)], the effect of the trigonal distortion within each manifold of bonding or antibonding bands is minimal and hence we disregard it compared to the other hopping param-

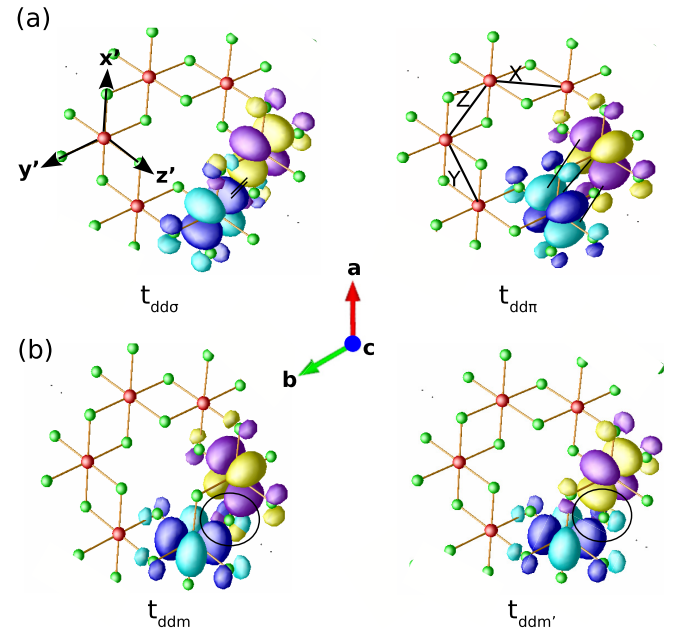


FIG. 5. Overlap of effective t_{2g} Wannier functions in the downfolded basis of ZrCl_3 , placed at two neighboring positions of Zr ions. Lobes of opposite signs are colored blue (yellow) and cyan (violet) for two different Zr ions. (a) Direct dd overlaps, with the left panel showing the head-on overlap ($dd\sigma$) and the right panel showing the lateral overlap ($dd\pi$). The overlaps are highlighted by lines. The t_{2g} orbitals are defined with the choice of local primed halogen-based coordinate systems, shown in the left panel. The X , Y , and Z M - M connecting bonds are shown in the right panel. The crystallographic coordinate system in terms of a , b , and c is also shown. (b) Indirect overlaps via the halogen site, between the same (left) and differently shaped (right) t_{2g} functions, labeled as ddm and ddm' in the text. Overlap region via halogen is encircled.

eters. The results, discussed in the following, are not influenced by this assumption, as has been explicitly checked.

With this, one can now write the first-NN hopping model for the t_{2g} orbitals as

$$H_{tb} = \sum_{\langle ij \rangle} \sum_{\alpha, \beta} \sum_{\eta \eta'} \Psi_{i\alpha\eta}^\dagger [h_{ij}^{\alpha\beta} \delta_{\eta\eta'}] \Psi_{j\beta\eta'}. \quad (1)$$

Here $\Psi_{j\alpha\eta}$ annihilates electrons at the j th site of the lattice with spin η ($=\uparrow, \downarrow$), in the orbital α ($=xy, yz, zx$). The h_{ij} is a 3×3 Hermitian matrix at the bond connecting the i th and the j th sites of the lattice as shown in Fig. 5(a).

Keeping in mind the different kinds of overlaps of the t_{2g} orbitals, we can write the h_{ij} matrix for the Z bond as

$$h_Z = \begin{pmatrix} t_{dd\sigma} & t_{ddm'} & t_{ddm'} \\ t_{ddm'} & t_{dd\pi} & t_{ddm} \\ t_{ddm'} & t_{ddm} & t_{dd\pi} \end{pmatrix} = t_{dd\sigma} h_\sigma + t_{dd\pi} h_\pi + t_{ddm} h_m + t_{ddm'} h_{m'}, \quad (2)$$

where $t_{dd\sigma}$, $t_{dd\pi}$, t_{ddm} , and $t_{ddm'}$ are hopping due to direct and indirect overlaps of the orbitals as discussed before. Also, h_σ ,

TABLE II. DFT estimated hopping terms defined for h_z matrix [cf. Eq. (2)] and SOC strength (λ). The last two rows show energy splitting in the t_{2g} level due to trigonal distortion. Apart from ratios, all the numbers quoted are in units of eV.

	TiX ₃			ZrX ₃			HfX ₃		
	F	Cl	Br	F	Cl	Br	F	Cl	Br
$t_{dd\sigma}$	-0.167	-0.220	-0.164	-0.546	-0.558	-0.476	-0.708	-0.666	-0.569
$t_{dd\pi}$	0.077	0.062	0.046	0.210	0.150	0.126	0.274	0.190	0.157
t_{ddm}	0.058	0.078	0.079	-0.061	0.030	0.038	-0.126	0.015	0.031
$t_{ddm'}$	-0.022	-0.030	-0.027	-0.023	-0.020	-0.020	-0.039	-0.022	-0.020
$t_{dd\pi}/t_{dd\sigma}$	-0.463	-0.281	-0.277	-0.385	-0.269	-0.264	-0.387	-0.285	-0.277
$t_{ddm}/t_{dd\sigma}$	-0.351	-0.357	-0.481	0.112	-0.053	-0.081	0.178	-0.022	-0.054
$t_{ddm'}/t_{dd\sigma}$	0.134	0.136	0.163	0.043	0.037	0.042	0.055	0.033	0.035
λ	0.015	0.028	0.040	0.030	0.043	0.043	0.060	0.152	0.152
$\lambda/t_{dd\sigma}$	-0.089	-0.127	-0.244	-0.055	-0.076	-0.090	-0.085	-0.228	-0.267
$\Delta = E_{e_g} - E_{A_{1g}}$	-0.030	0.050	0.039	-0.178	0.057	0.077	-0.212	0.065	0.088
$\Delta/t_{dd\sigma}$	0.180	-0.227	-0.236	0.325	-0.103	-0.161	0.300	-0.097	-0.154

h_π , h_m , and $h_{m'}$ are 3×3 matrices given by

$$\begin{aligned}
 h_\sigma &= \begin{pmatrix} 1 & 0 & 0 \\ 0 & 0 & 0 \\ 0 & 0 & 0 \end{pmatrix}, & h_\pi &= \begin{pmatrix} 0 & 0 & 0 \\ 0 & 1 & 0 \\ 0 & 0 & 1 \end{pmatrix}, \\
 h_m &= \begin{pmatrix} 0 & 0 & 0 \\ 0 & 0 & 1 \\ 0 & 1 & 0 \end{pmatrix}, & h_{m'} &= \begin{pmatrix} 0 & 1 & 1 \\ 1 & 0 & 0 \\ 1 & 0 & 0 \end{pmatrix}. \quad (3)
 \end{aligned}$$

The form of the hopping of the X and Y bonds can be obtained by exploiting the threefold rotation symmetry of the lattice, as detailed in the Appendixes.

The DFT estimates for the hopping amplitudes, $t_{dd\sigma}$, etc., for different materials are given in Table II. For different materials, the generic hierarchy of the relative strengths of the hopping parameters are found to be as follows:

$$|t_{dd\sigma}| > |t_{dd\pi}| \gg |t_{ddm}| \geq |t_{ddm'}|. \quad (4)$$

The low-energy effective tight-binding model can be obtained by adding atomic SOC to Eq. (1):

$$H = \sum_{(ij)} \sum_{\alpha\beta} \sum_{\eta\eta'} \Psi_{i\alpha\eta}^\dagger [h_{ij}^{\alpha\beta} \delta_{\eta\eta'} - \tilde{\lambda} \mathbf{I}_{\alpha\beta} \cdot \mathbf{s}_{\eta\eta'} \delta_{ij}] \Psi_{j\beta\eta'}, \quad (5)$$

where $\lambda (>0)$ is the strength of SOC and \mathbf{I} 's represent the three $l = 1$ orbital angular momentum matrices while \mathbf{s} are the Pauli matrices that represent the spin degrees of freedom of the electrons. To estimate the SOC in the studied materials, we calculated the band structure within GGA+SOC. The tight-binding fit of the obtained band structure with DFT-derived hopping integrals together with a tunable λ was used to extract the best-fit λ value of a given compound. The estimated λ values are listed in Table II.

For understanding of the generic structure of the non-interacting phase diagram in the context of the different compounds and possibly others, it is useful to scale out an overall energy scale, $\mathcal{E} = |t_{dd\sigma}| + |t_{ddm}|$, and study the rescaled Hamiltonian in terms of dimensionless coupling constants. To this end, it is useful to rewrite Eq. (5) as

$$\mathcal{H} = \mathcal{E} \sum_{(ij)} \sum_{\alpha\beta} \sum_{\eta\eta'} \Psi_{i\alpha\eta}^\dagger [H_{ij}^{\alpha\beta} \delta_{\eta\eta'} - \tilde{\lambda} \mathbf{I}_{\alpha\beta} \cdot \mathbf{s}_{\eta\eta'} \delta_{ij}] \Psi_{j\beta\eta'}, \quad (6)$$

such that H_{ij} can be obtained by rescaling h_{ij} [Eq. (1)] and in particular its form on the Z bond is obtained by rescaling Eq. (2) as

$$H_Z = -(1 - \tau_m)h_\sigma + \rho\tau_m h_m + r(1 - \tau_m)h_\pi + \tau'_m h_{m'} \quad (7)$$

with

$$\begin{aligned}
 t_{dd\sigma} &= -\mathcal{E}(1 - \tau_m), & t_{dd\pi} &= r t_{dd\sigma}, & t_{ddm} &= \rho\mathcal{E}\tau_m, \\
 t_{ddm'} &= \mathcal{E}\tau'_m, & \lambda &= \mathcal{E}\tilde{\lambda}. \quad (8)
 \end{aligned}$$

The description of the model Hamiltonian, defined in terms of \mathcal{E} , τ_m , r , ρ , and τ'_m , besides being helpful in providing a unified description of different compounds, is advantageous for (i) the ease of interpolating between direct- and indirect-hopping-dominated situations by varying only τ_m , and (ii) arriving at a phase diagram in two-variable $\tilde{\lambda}$ - τ_m space.

The parameter $\rho = \pm 1$ additionally indicates that the indirect hopping amplitude t_{ddm} can be of either sign. In particular we find that (see Table II) ZrF₃ and HfF₃ have $\rho = -1$, making the situation markedly different from that of chlorides and bromides, which was already hinted from the band structure (see Fig. 3). This distinct difference of the fluorides arises from the following characteristic features of F: (1) much smaller ionic radius (147 pm), and (2) much higher electronegativity (3.98), compared to chlorine and bromine with ionic radii (electronegativities) of 175 pm (3.16) and 185 pm (2.96), respectively. Since none of the fluoride compounds have been so far synthesized, for the rest of this paper, we are concerned with $\rho = +1$ and take up the case for fluorides towards the end in Sec. VII.

VI. SINGLE-ELECTRON PHASE DIAGRAM

The Hamiltonian in Eq. (6) leads to a rich set of possibilities even at the noninteracting level which crucially decide the fate of electron-electron interactions and the low-energy phases. While in actual materials all the parameters are present, we unfold the story in steps, by following the hierarchy of different energy scales and introducing them one by one. This provides understanding at the model level of the influence of each distinct hopping terms in the resulting phases. It is interesting to note though that the phases

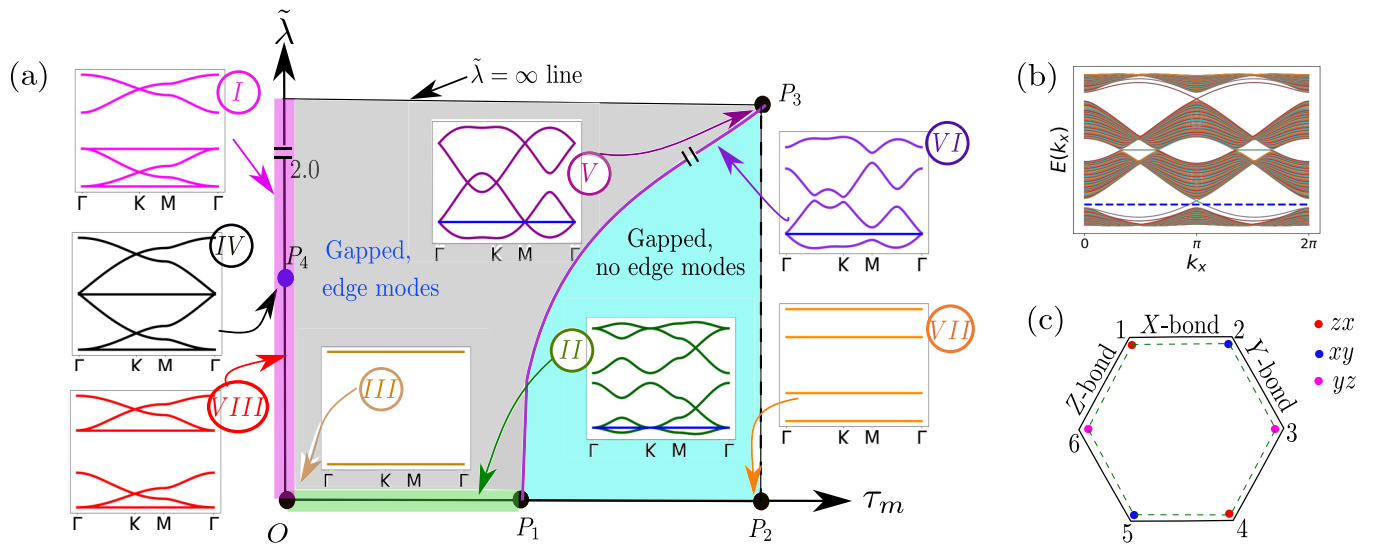


FIG. 6. (a) Phase diagram in the τ_m - $\tilde{\lambda}$ plane for $r = 0$, $\tau'_m = 0$, and $\rho = +1$. The two gapped phases are shown with different colors (gray and cyan). The vertical axis is plotted between $\tilde{\lambda} \in [0, 2.0]$. For larger values, no new phases appear and this feature for very large $\tilde{\lambda} (\rightarrow \infty)$ is shown through extrapolation as shown by the break lines on the vertical axis. The band structures, plotted along the Γ , K, and M points of the BZ at different points on the phase diagram are shown as insets. The blue horizontal lines in insets II, V, and VI show the position of the Fermi level. In inset II, both the bands are sixfold degenerate as explained in the text. Insets V and VI are for very large values of $\tilde{\lambda}$ and hence only the four lower-energy $J = 3/2$ bands are shown. (b) Band structure in the topological gapped phase (for $\tau_m = 0.9$, $\tilde{\lambda} = \infty$, $r = 0$, and $\tau'_m = 0$) in cylindrical geometry. The edge modes at the Fermi energy are shown by the blue solid line, with Fermi level marked with a dashed line. (c) A single hexagon showing the origin of molecular orbitals at point P_2 of the phase diagram in (a). Different colored dots represent three t_{2g} orbitals. The six sites of the hexagon are labeled with numbers from 1 to 6. The symmetric linear combination of the orbitals connected by the green dotted line forms the lowest energy band. Other orbitals are localized on single bonds of the hexagon, shown by black dotted lines. See text for details.

corresponding to the complex hopping model of actual materials are connected to the Dirac semimetallic phase of the idealized SU(8) model, and can be achieved by change of $\tilde{\lambda}$ and τ_m .

A. Phase diagram for τ_m - $\tilde{\lambda}$ model

Our first-principles calculations show that the major deviation from the indirect hopping model discussed in Refs. [18,19] is the direct hopping given by $t_{dd\sigma}$. The simplest model, therefore, consists of $t_{dd\sigma}$, t_{ddm} , and λ , setting the other subleading terms, $t_{dd\pi}$ and $t_{ddm'}$, to zero. This gives rise to a phase diagram in the τ_m - $\tilde{\lambda}$ plane, such that $\tau_m = 0$ (1) corresponds to the purely direct (indirect) hopping limits at different values of SOC with $r = \tau'_m = 0$. Having discussed this phase diagram of the minimal possible model, capturing the interplay of direct and indirect hopping, we next sequentially turn to $t_{dd\pi}$ and $t_{ddm'}$, and examine the τ_m - $\tilde{\lambda}$ phase diagram by first setting $r = -0.3$, and then setting $\tau'_m = -\tau_m$. We note that the importance of direct metal-metal interaction, over the conventional description of ligand-mediated interaction in the description of the phenomenology of transition-metal compounds, has been acknowledged recently, in the context of cobaltates [42].

1. τ_m - $\tilde{\lambda}$ phase diagram with $r = \tau'_m = 0$

The phase diagram in the τ_m - $\tilde{\lambda}$ plane is shown in Fig. 6(a). The top right corner, $P_3 (\equiv (\tau_m = 1, \tilde{\lambda} = \infty))$, corresponds to infinite SOC in the purely indirect hopping limit with infinite coupling. This, for d^1 , gives rise to an SU(8) DSM as

discussed in Ref. [19]. At P_3 , the six t_{2g} orbitals (including spin degeneracy) split up into four $J = 3/2$ and two $J = 1/2$ orbitals, which are separated by an infinite energy gap ($\propto \tilde{\lambda}$) with the $J = 3/2$ orbitals being of lower energy. Hence at this point we obtain quarter filled $J = 3/2$ orbitals whose band structure is shown in inset V of Fig. 6(a). Here, the lowest band linearly touches the upper band at the Γ and the M points of the BZ, giving rise to four 4-component Dirac fermions sitting at four valleys: the three M points of the BZ and one at the Γ point that constitutes the SU(8) DSM [19]. Remarkably, almost the entire phase diagram, except the pink and green shaded parts along the $\tau_m = 0$ and $\tilde{\lambda} = 0$ axes, can be understood from this SU(8) limit as we now discuss.

On moving away from the SU(8) point, all the Dirac fermions get gapped out, generically giving rise to band insulators. However, the nature of these two band insulators obtained in the two extreme limits of changing τ_m or $\tilde{\lambda}$ away from P_3 are different. One of them—that obtained by varying only τ_m —is a free fermion SPT phase [22], as is evident from the gapless edge modes plotted in Fig. 6(b). These edge modes are protected by time-reversal symmetry. Indeed out of the 24 distinct ways of gapping out the SU(8) Dirac fermions discussed in Ref. [19], there are precisely two different time-reversal-invariant lattice (\mathcal{A}_{1g}^e) singlet masses where we have used the notations of Ref. [19] for ready reference. The above two band insulators correspond to these two singlets as detailed in the Appendixes. The two insulating phases are separated by a phase transition denoted by the magenta curve connecting the points P_3 and $P_1 (\equiv (\tau_m = 0.67, \tilde{\lambda} = 0))$. On this line, only the Dirac fermions at the Γ point become

gapless while those at the three M points remain gapped across the transition as shown in the band structure (inset VI) in Fig. 6(a). The resultant theory has an enhanced SU(2) symmetry as detailed in the Appendixes.

In Fig. 6(a), diametrically opposite to P_3 is the point $O \equiv (\tau_m = 0, \tilde{\lambda} = 0)$, which describes the purely direct hopping model via $t_{dd\sigma}$ without SOC. Here, the hopping Hamiltonian [Eq. (6)] reduces to a particularly simple form, given by

$$H = -\mathcal{E} \left(\sum_{(ij) \in Z\text{-bonds}} \Psi_{i,xy,\eta}^\dagger \Psi_{j,xy,\eta} + \sum_{(ij) \in X\text{-bonds}} \Psi_{i,yz,\eta}^\dagger \Psi_{j,yz,\eta} + \sum_{(ij) \in Y\text{-bonds}} \Psi_{i,zx,\eta}^\dagger \Psi_{j,zx,\eta} \right) + \text{H.c.}, \quad (9)$$

such that on the Z, X, and Y bonds [see Fig. 5(a)] respectively only the xy , yz , and zx orbitals hop. Since each set of bonds forms a disconnected network of dimers that rotates into itself under C_3 , we get bonding and antibonding orbitals of the respective types on each of the three bonds resulting in two sets of sixfold-degenerate (including spin $\eta = \uparrow, \downarrow$) flat bands as shown in inset III of Fig. 6(a). This is evident in the form of the Wannier functions obtained from DFT (cf. Fig. 5). This kind of separation of the energy bands into two groups of three bands is also seen in the DFT band structures of ZrCl_3 shown in Fig. 2(c), which is dominated by the direct overlap $t_{dd\sigma}$ as given in Table II.

The fact that the entire OP_1 segment on the $\tilde{\lambda} = 0$ line is gapless is expected on very general grounds and is in fact dictated by the general structure of the phase diagram starting from the SU(8) symmetric point, P_3 . This can be rationalized based on the fact that on this line there is an enhanced SU(2) spin rotation symmetry such that this line cannot be a part of the free fermion SPT phase lying above it for finite $\tilde{\lambda}$ —as predicted by the SU(8) theory. The trivial insulating phase [shown in cyan in Fig. 6(a)] of course can be connected to the spin-rotation-symmetric segment P_1P_2 continuously. Finally at the point $P_2 \equiv (\tau_m = 1, \tilde{\lambda} = 0)$, the bands become flat again with a degeneracy of 2-4-4-2 [inset VII of Fig. 6(a)]. At this point (P_2), the lowest band is made up of spin-degenerate *molecular orbitals* of the type shown in Fig. 6(c) at each hexagon. On deviating from this point, these orbitals acquire dispersion. Hence the entire gapped trivial insulator [shown in cyan in Fig. 6(a)] can be understood in terms of these effective eigenmodes.

On increasing the SOC ($\tilde{\lambda}$) along the $\tau_m = 0$ line in Fig. 6(a), the sixfold symmetry is independently lifted in the bonding and antibonding sectors without intermixing for small $\tilde{\lambda}$ as shown in inset VIII of the figure. The band structure (inset VIII) is very similar to that of monolayer kagome band structure [43]—for both the bonding and antibonding sectors—with the lower dispersing band touching the flat band quadratically at the Γ point of the BZ. As one increases the SOC, the bandwidth of each of the two sectors increases while they retain their overall shape such that at the point $P_4 \equiv (\tau_m = 0, \tilde{\lambda} = 1.35)$ the bands touch at the Γ point leading to a spin-1 Dirac dispersion [44] at the touching of the two sectors [inset IV of Fig. 6(a)]. On increasing SOC further, remarkably the second flat band—previously associated with

the antibonding sector—detaches from it and becomes a part of the bonding sector, leading to a division of four lower bands and two higher bands [inset I of Fig. 6(a)], as expected from the $J = 1/2$ and $J = 3/2$ splitting of the atomic orbitals at large SOC. For d^1 materials, however, the above change of band structure is not important as only the lowest flat band is filled such that the chemical potential lies at the lowest quadratic band touching points leading to a very unstable (to interactions) quadratic band-touching semimetal with one of the flat bands having divergent effective mass.

The above structure of the phase diagram gives a good starting point to connect to the DFT band structure by incorporating the subleading interactions that we now turn to discuss. Two such important subleading parameters are $t_{dd\pi}$ and $t_{ddm'}$ representing the subleading direct and indirect hopping, respectively [see Eqs. (2) and (8) as well as Table III]. We study their effects as a buildup to the material phase diagram.

2. Effect of $t_{dd\pi}$

The first subleading hopping that is relevant across all the compounds is the direct hopping via the π overlap, denoted by $t_{dd\pi}$ as shown in Fig. 5 and incorporated via the parameter $r = t_{dd\pi}/t_{dd\sigma}$ in our effective tight-binding Hamiltonian [Eq. (6)], as shown in Eq. (8). However, instead of scanning the entire phase diagram as a function of r , we confine ourselves to $r = -0.3$ —a value which is roughly consistent for the different materials. The resultant phase diagram is shown in Fig. 7.

The P_2P_3 line of Fig. 7(a) is exactly equivalent to that of Fig. 6(a) and hence the description of the entire trivial gapped band insulator in the cyan region remains the same apart from the quantitative renormalization of the band structure away from the $\tau_m = 1$ line. Similarly the physics of the $\tilde{\lambda} = \infty$ for $\tau_m < 1$ holds until the point P_7 , giving rise to the Z_2 free fermion SPT phase (gray region) with gapless edge modes, exactly in the case of $t_{dd\pi} = 0$ in Fig. 6(a). The intermediate line, P_3P_6 , hence is associated with a Dirac band touching at the Γ point of the BZ giving rise to an SU(2) DSM. However, the effect of $t_{dd\pi} = r|t_{dd\sigma}| \propto (1 - \tau_m)$ drastically rearranges the band structure for lower τ_m , as we discuss now.

The $t_{dd\pi}$ lifts the threefold degeneracy of the flat bands at the point $O = (\tau_m = 0, \tilde{\lambda} = 0)$, leading to dispersive bands that cross the chemical potential, giving rise to a compensated band metal such that the net Luttinger volume is zero. The relevant Fermi surface is named $F1'$ and is shown in Fig. 7(b). However, this is highly unstable due to the touching of the hole and particle Fermi pockets and, on increasing both τ_m and $\tilde{\lambda}$, the resultant Fermi surface undergoes topological changes giving rise to a plethora of compensated band metals denoted by $F1-F11$ in Fig. 7(a). The intervening Lifshitz transitions [45,46] include cases where both separate sheets of Fermi surfaces merge, e.g., $F4$ to $F5$ via van Hove singular necks, as well as instances where individual sheets of Fermi surfaces disappear, e.g., $F1$ to $F4$. This generic appearance of the compensated band metals with diverse Fermi-surface topology is particularly relevant to the materials under consideration as we discuss in the next section in detail along with the relevant Lifshitz transitions.

We would like to end this discussion about the effect of $t_{dd\pi}$ by commenting on the metals $F1-F11$ [Fig. 7(a)] that

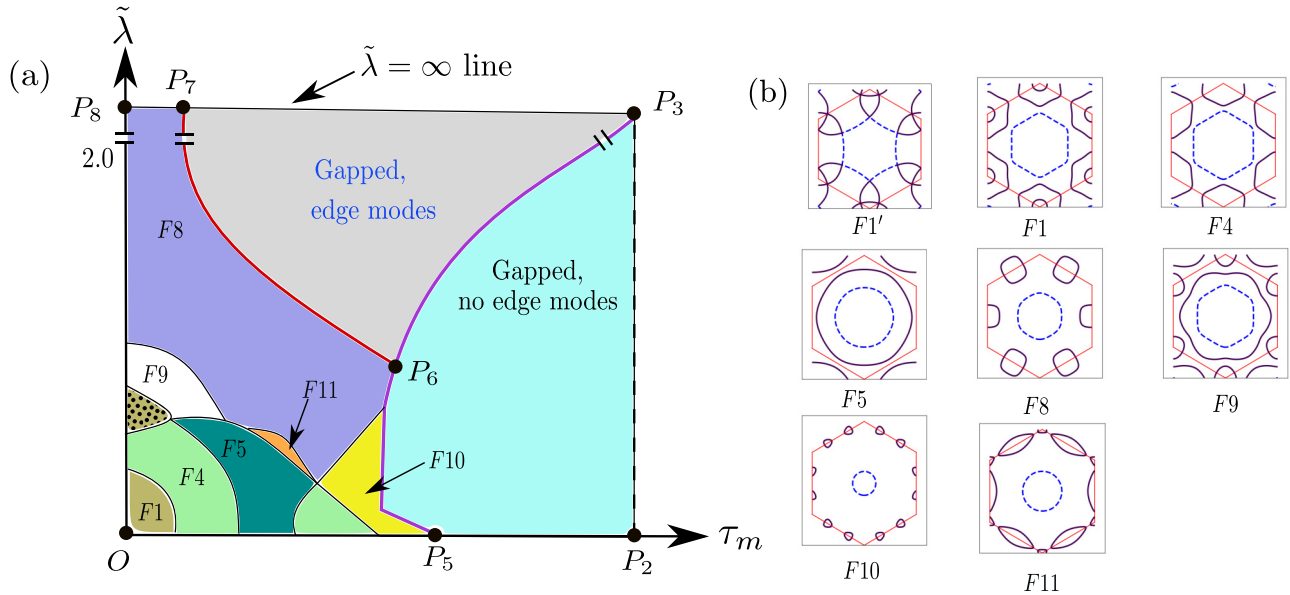


FIG. 7. (a) Phase diagram for $\rho = +1$, $r = -0.3$, and $\tau'_m = 0$. Two gapped phases shown in gray and cyan shading. The different metallic phases are shown with different colors and labeled as $F1, \dots, F11$. (b) Fermi surfaces corresponding to different metallic phases. The hole-like Fermi surfaces are shown with blue dashed lines and the electron-like Fermi surfaces are shown with solid violet lines. The hexagonal BZ is shown with red solid lines. The $F1'$ Fermi surface corresponds to the O point of the phase diagram shown in (a). The solid and dotted regions of $F1$ differ by the fact that, for the Fermi surface corresponding to the dotted region, one of the Fermi pockets around the K points is electron-like and the other is hole-like, while both are electron-like for the solid region.

occupy the region that was erstwhile [Fig. 6(a)] a part of the topological insulator. Interestingly for $F8$, the electron bands evolve continuously from the free fermion SPT phase and hence it inherits a nontrivial Z_2 invariant for the bands crossing the chemical potential. In fact, except on the $\tilde{\lambda} = 0$ line, we find that for all the metals in the phase diagram under consideration, one of the bands crossing the chemical potential has nontrivial Z_2 index, calculated following the method discussed in Ref. [47]. The method is applicable for systems with inversion symmetry, as in the present case.

3. Effect of $t_{ddm'}$

We now turn to the effect of the indirect hopping mediated by $t_{ddm'}$ on the minimal model with phase diagram in Fig. 6(a). Again we choose a representative value of $t_{ddm'} = -t_{ddm}$ —in the regime relevant to the materials—to indicate its effect. Unlike $t_{dd\pi}$, this indirect hopping now drastically reorganizes the $\tau_m \approx 1$ region of the phase diagram, apparent by contrasting Fig. 6(a) with Figs. 7(a) and 8.

In particular the line $\tau_m = 0$ remains unaltered with respect to the minimal model (Fig. 6). Also the free fermion SPT phase (in gray in Fig. 8) is stable to finite $t_{ddm'}$, albeit it does not extend all the way to the point P_3 . In fact the $SU(8)$ Dirac point (P_3) now develops into a compensated band metal as the Dirac cones, at the erstwhile P_3 point, move away from the chemical potential in the opposite direction—the Dirac node at the Γ point moves above it and those at the M points move below it—giving rise to Fermi pockets around these points. The band structure at the P_3 point is shown in inset II of the phase diagram in Fig. 8. The resultant Fermi surface around this point is of $F8$ type given in Fig. 7(b).

As we move away from the P_3 point along the $\tilde{\lambda} = \infty$ line by decreasing τ_m (thus increasing $t_{dd\sigma}$), the $F8$ Fermi surface continues to exist, although a finite gap at the M and the Γ points opens up (away from the chemical potential) between the lowest and the second lowest band. This gap opening due

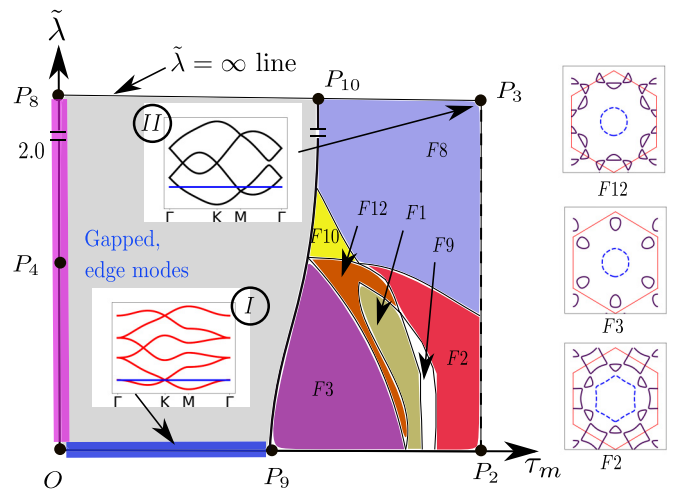


FIG. 8. Phase diagram for $r = 0$, $\tau'_m = -\tau_m$, and $\rho = +1$. Inset I shows a prototypical band structure for a point on the OP_9 line where the lowest band touches the next band linearly at the K points, while inset II shows the band structure at the P_3 point. Since $\tilde{\lambda} = \infty$ at P_3 , only four bands ($J = 3/2$ bands) are shown in inset II. As in Fig. 7(a), metallic phases with different Fermi surface topology are labeled and colored. In addition to $F8, F9,$ and $F10$, introduced in Fig. 7(a), three new phases, labeled as $F2, F3,$ and $F12$, appear. The Fermi surface topology for $F2, F3,$ and $F12$ phases are shown on the right-hand side.

to the effect of $t_{dd\sigma}$ gives a nontrivial Z_2 number to the lowest band and hence the $F8$ metal in the phase diagram in Fig. 8 is a topological metal. On moving further away from the P_3 point along the $\tilde{\lambda} = \infty$ line, the size of the Fermi pockets of the $F8$ metal continuously shrinks and eventually vanishes at the P_{10} point, after which the system enters into a gapped phase. Since this transition from the $F8$ metal to the gapped phase does not happen through a band touching, the Z_2 invariant of the lower band remains unchanged across this transition and hence the gapped phase is also a topological insulator—the same free fermion SPT phase as in Fig. 6.

Turning to low SOC, the P_2 point no longer has flat bands but now gains a dispersion due to τ'_m leading to a compensated metal of Fermi surface type $F2$ as shown in Fig. 8. On moving from the point away from the P_2 point along the $\tau_m = 1$ line, the $F2$ Fermi surface transforms into an $F8$ -type Fermi surface, which is then connected to the P_3 point. This $F8$ - $F2$ transition does not involve any band touching, but just a change of the chemical potential, and hence the $F2$ region of the phase diagram is also a topological metal. On reducing the values of τ_m from the point P_2 , the system encounters various other metallic phases which have different Fermi surfaces ($F9$, $F1$, $F12$, $F3$, etc.). We find that for all these phases, the bands crossing the Fermi energy always have a nontrivial Z_2 index. Thus, all the metals in this phase diagram are also topological metals.

Finally, on the line OP_8 , $\tau_m = \tau'_m = 0$ and hence the description of this line is the same as in the phase diagram in Fig. 6. On the other hand, along the OP_9 line (for which $\tilde{\lambda} = 0$), the lowest band touches the upper band linearly at the K points. The effect of finite $\tilde{\lambda}$ opens up a gap at the K points and the system enters into the topological gapped phase (gray shaded region).

B. The material phase diagram

Having discussed the minimal tight-binding model and the effect of the subleading hopping terms resulting in a rich single-particle phase diagram, we now turn to the regime that may be most suited to the material parameters, except for the fluorides. To this end we choose the representative hyperplane given by $\rho = +1$, $r = 0.3$, and $\tau'_m = -\tau_m$ and vary $\tau_m \in (0, 1)$ and $\tilde{\lambda} \in (0, \infty)$.

The phase diagram in this parameter regime is shown in Fig. 9. Due to the complementary effects of the secondary direct and indirect hopping ($t_{dd\pi}$ and $t_{ddm'}$, respectively), the resultant phase diagram is in a way a superposition of Figs. 8 and 7(a) such that all the phases appearing in this case are gapless, are perfectly compensated, and have Fermi surfaces with at least one partially filled band having nontrivial Z_2 invariant.

Based on which particular band(s) carry nontrivial Z_2 , the phase diagram can be demarcated by red, magenta, and blue lines (see Fig. 9). The Z_2 index for the lowest band is nonzero for the region of the phase diagram which is on the right-hand side of the red solid line. On the other hand, the second lowest band has nontrivial Z_2 index for the regions of the phase diagram which are either left of the red solid line or right of the magenta solid line. On the red line, the lowest and the second lowest bands touch at the M point and the Z_2 character

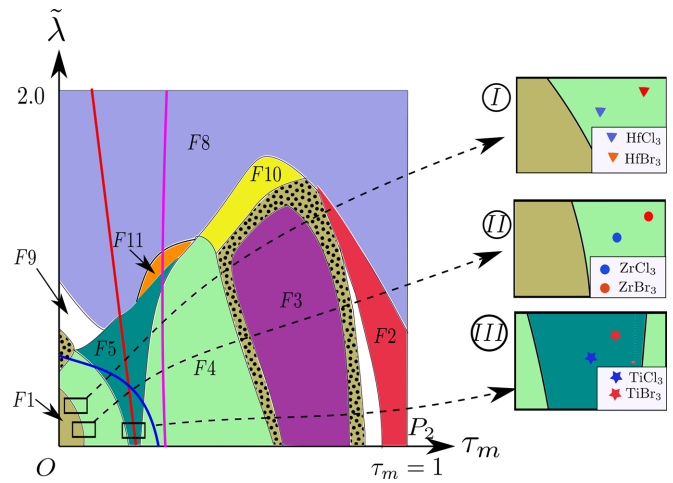


FIG. 9. Phase diagram for $\rho = +1$, $r = -0.3$, and $\tau'_m = -\tau_m$ with $0 \leq \tau_m \leq 1$ and $0 \leq \tilde{\lambda} \leq 2.0$. For $\tilde{\lambda} > 2.0$, the $F8$ phase continues to exist. The six different chloride and bromide compounds are placed in this phase diagram, according to the estimated parameter values of the low-energy Hamiltonian (cf. Table II), shown in insets I, II, and III. The phase diagram is demarcated by the red, blue, and magenta lines, according to the Z_2 characters of the bands. See text for details.

of the two bands switches. On the magenta line, the second lowest band touches the third lowest band and thus encounters another change in Z_2 character. The third lowest band, which crosses the Fermi energy only at the $F1$ region which is near the origin O , has nontrivial Z_2 index for the region which is left of the blue solid line in the phase diagram. On this blue line, the third lowest band touches the fourth lowest band and encounters a change in Z_2 character.

The positioning of the materials ZrX_3 , TiX_3 , and HfX_3 ($X = \text{Cl}, \text{Br}$) in the phase diagram, based on the estimated parameters given in Table II, is shown in zoomed plots given in Fig. 9. Due to weaker SOC compared to the strength of leading hopping interactions, the studied compounds are all placed towards the bottom of the phase diagram. Given the fact that $t_{dd\sigma}$ (t_{ddm}) is significantly larger (smaller) in Zr and Hf compounds compared to Ti compounds, as expected, Zr and Hf compounds are placed to the left of the Ti compounds. Given the similarity in electronic structure of Zr and Hf compounds (see Fig. 3), it is not surprising that they belong to the same $F4$ class, with Hf compounds lying higher in position compared to Zr, due to stronger SOC. On the other hand, Ti compounds belong to the distinctly different $F5$ class. Systematically, bromine compounds lie higher than and to the right of chlorine compounds, due to stronger SOC and weaker direct hopping strength, respectively.

The detailed Fermi surfaces (FSs) of the compensated, topological metallic phases of the six compounds are shown in Fig. 10. The $F4$ -type FS of ZrX_3 and HfX_3 compounds is characterized by three disjoint Fermi pockets: two electron-like pockets around the two K points and one hole-like pocket around the Γ point. On the other hand, the TiX_3 compounds having $F5$ -type FSs have two Fermi pockets, one electron-like and one hole-like around the Γ point.

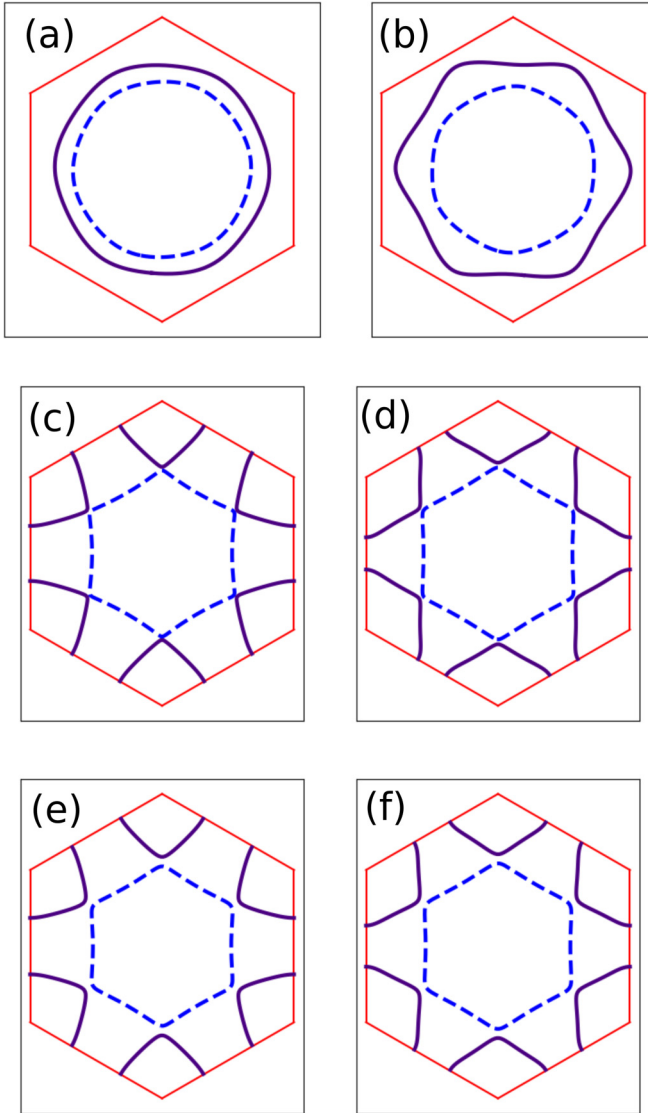


FIG. 10. Fermi surfaces for (a) TiCl_3 , (b) TiBr_3 , (c) ZrCl_3 , (d) ZrBr_3 , (e) HfCl_3 , and (f) HfBr_3 . Diagrams (a) and (b) are $F5$ -type Fermi surfaces while the rest are of $F4$ type. The blue dotted lines show hole-like Fermi surfaces and the solid indigo lines show electron-like Fermi surfaces. The red line shows the boundary of the hexagonal BZ.

C. Nesting and Lifshitz transitions

A characteristic feature of some of the FSs in Fig. 10 are the flattish *almost nested* sections—involving both intra- and interpockets. This makes them particularly susceptible to nesting instabilities in the presence of electron-electron interactions at appropriate wave vectors. Our preliminary results indeed indicate enhanced susceptibilities in the charge-density-wave channel due to such nesting. The detailed characterization of such instabilities though require more accurate study particularly due to the intricate structure of the FSs involved.

Another feature of the phase diagram is the presence of a plethora of Lifshitz phase transitions [45,46] between the variety of compensated metals (Fig. 9). These phase transitions involving a change in the Fermi surface topology can

be classified into two broad categories [45,48]: (1) a *pocket vanishing* type, associated with the disappearance of new segments of Fermi surface, e.g., between $F1$ and $F4$ where the Fermi pockets centered around the BZ corners appear, possibly relevant for $\text{Zr}(\text{Hf})\text{Cl}_3$ and $\text{Zr}(\text{Hf})\text{Br}_3$, and (2) a *neck collapsing* type associated with merging of two segments of Fermi surfaces, e.g., the transition between $F4$ and $F5$ where two particle-like Fermi pockets develop a neck that meets at the M points, possibly relevant for TiCl_3 and TiBr_3 . These transitions, accessed in the present case by tuning the band parameters at a particular filling, occur due to the change of the band structure at the chemical potential. While the former leads to a step function in the single-particle density of states, $\rho(\epsilon - \epsilon_F) \sim \theta(\epsilon - \epsilon_F)$, the latter has a logarithmic singularity, i.e., $\rho(\epsilon - \epsilon_F) \sim -\ln|\epsilon - \epsilon_F|$ and hence has a van Hove singularity arising from the vanishing Fermi velocity for the electrons on the Fermi surface. This singular behavior can be reflected in thermodynamic measurements such as magnetic susceptibility [48] as well as scaling of bipartite entanglement entropy [49]. Interestingly, the tuning of the band parameters can be achieved through biaxial straining which should be achievable considering the layered structure of the materials similar to SrRuO_4 [50]. Considering about 2% compressive strain on ZrCl_3 , the direct $dd\sigma$ hopping is found to be enhanced by about 20% while the indirect hopping is found to be heavily suppressed and thereby conducive to triggering an $F4 \rightarrow F1$ transition. This may be even easier for Hf compounds, which are even closer to the $F4$ - $F1$ boundary. Our DFT-calculated FS for a 1% strained Hf compound indeed shows an $F1$ type. Straining on Ti compounds shows a similar effect, although the percentage change is found to be much smaller. Therefore, such straining may be of interest in investigating the physics of the Lifshitz transition.

VII. $\rho = -1$: IMPLICATION FOR FLUORIDES

Having discussed the situation with the chlorides and the bromides, we now turn to fluorides, which as indicated above (cf. Table II) show markedly different electronic structure. Furthermore, unlike chlorides and bromides, the tight-binding parameters for fluorides show diverse behavior even among the $3d$, $4d$, and $5d$ transition metals, the parameters for Ti being rather different from that of Zr and Hf. This hinders providing a universal framework to describe the three fluoride compounds, captured through a common phase diagram, as was possible for chlorides and bromides. We thus concentrate on the most striking difference between Zr and Hf chlorides and bromides, and Zr and Hf fluorides, namely, the change in sign of the indirect hopping, t_{ddm} , captured by the parameter ρ in Eq. (8). This affects some of the basic conclusions stemming from the structure of the minimal phase diagram, presented in Fig. 6. In the following, we thus confine ourselves to the τ_m - $\tilde{\lambda}$ phase diagram, which determines the nature of the low-energy single-particle starting point for these materials, without delving into the complexity of the subleading hopping like $t_{dd\pi}$ and t_{ddm} . The obtained results are shown in Fig. 11, which should be contrasted with Fig. 6(a).

First of all, we notice a similarity of the phase diagrams in Figs. 11 and 6(a), especially for large $\tilde{\lambda}$. This apparent similarity, however, hides an important contrast that can be

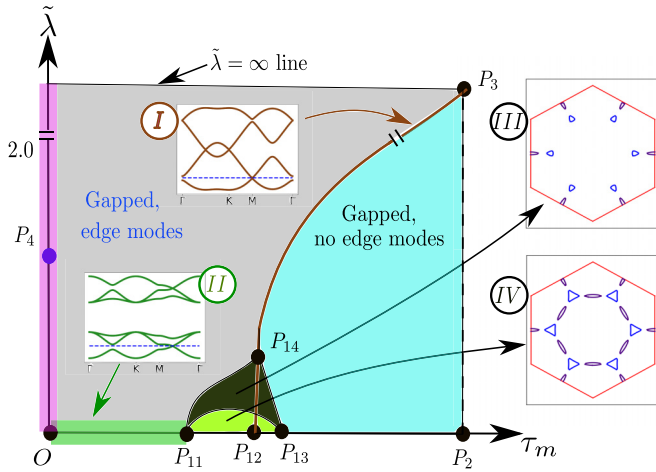


FIG. 11. τ_m - $\tilde{\lambda}$ phase diagram with $\rho = -1$, $r = 0$, and $\tau'_m = 0$. The two gapped phases, shaded as gray and cyan, as well as pink lines in the phase diagram are identical to those in Fig. 6(a). The band structures on a typical point on the OP_{11} line are shown in inset II. Inset I shows the band structure on the transition line between the two gapped phases. Note that inset I shows only four bands since it is drawn for a large value of $\tilde{\lambda}$ where the four lower-energy $J = 3/2$ orbitals are separated from the higher-energy $J = 1/2$ orbitals by a large energy separation. As opposed to Fig. 6(a), this phase diagram hosts two topological metallic phases, marked in lime green and dark green. The Fermi surfaces for the two metallic regions are shown by insets III and IV.

best understood as follows. Starting from the SU(8) limit, P_3 in the present case, is a *particle-hole* inverted version of Fig. 6(a) due to the change in sign of t_{ddm} . Thus, while P_3 still gives an SU(8) DSM with four 4-component Dirac points at Γ and three M points, the associated spinors are not necessarily the same as in the previous case, but are related to it via a microscopic particle-hole transformation. In fact this theory is therefore a particle-hole conjugate version of the SU(8) metal discussed in Ref. [19] and hence the same mass analysis can be applied to the present case. It is for this reason we still have the same two gapped phases—the free fermion topological and trivial band insulators on deviating away from the SU(8) semimetal—resulting from the two lattice singlet masses [19]. However, the difference in the eigenmodes due to the change in sign becomes apparent at the transition between the two insulators, which now is brought about by closing of the gap at the three M points on the line P_3P_{14} while that at the Γ point remains gapped—unlike the case for the P_3P_1 line in Fig. 6(a). This leads to an enlarged SU(6) internal symmetry for the $N_F = 3$ free Dirac fermions on the P_3P_{14} line (see Appendix E.4).

Another consequence of the above change in the nature of the spinors is the appearance of additional compensated semimetals for lower values of $\tilde{\lambda}$ around $t_{dd\sigma} \sim t_{ddm}$. The corresponding Fermi surfaces are shown in insets III and IV. The lowest bands of these metals have nonzero Z_2 index on the closed region $P_{11}P_{12}P_{14}$, while the upper band is Z_2 trivial. On the line $P_{12}P_{14}$, the lowest band touches the upper band at the M points and the Z_2 indices of these two bands switch. Thus, one of the bands of these metals always has nonzero Z_2 index and these are topological metals. On the $P_{13}P_{14}$ line,

Fermi pockets of the metals shrink to zero and the system enters the trivial insulating phase. Hence, the change of sign of the indirect hopping makes the situation more favorable to the topological metallic phase, which may be stabilized even without the inclusion of subleading hopping terms.

VIII. SUMMARY AND OUTLOOK

In summary, following the stimulating proposal of achieving an SU(8) DSM state in quarter-filled $J = 3/2$ spin-orbit-coupled electrons, we critically examine the material realization of this proposal considering d^1 transition-metal trihalide family of compounds, MX_3 . Systematic variation of both the metal site from $3d$ to $5d$ ($M = \text{Ti, Zr, Hf}$) as well as the halide site from $2p$ to $4p$ ($X = \text{F, Cl, Br}$) allows to study the interplay of different microscopic energy scales. Although only three out of the studied nine compounds have been synthesized so far, we do hope our study will encourage synthesis of other compounds too.

Our first-principles electronic structure calculations in combination with minimal tight-binding models show that a hierarchy of electron hopping pathways is needed to faithfully capture the rich low-energy single-electron physics in these compounds. Importantly, our study uncovers the dominant role of direct metal-metal hopping. Thus, a minimum of five band parameters—atomic SOC (λ), two direct metal-metal hoppings ($t_{dd\sigma}, t_{dd\pi}$), and two indirect metal-halide-metal hoppings ($t_{ddm}, t_{ddm'}$)—dictate the low-energy fermiology. Our study further unravels that, while the chlorides and bromides have a generic trend of band parameters, the fluorides are distinct, due to the drastic difference in the size and electronegativity of the fluoride ion compared to chloride and bromide.

Inclusion of this material-specific reality renders the physics of the above candidate compounds in a domain far removed from the idealized SU(8) DSM. Instead, a variety of topologically nontrivial compensated metals get stabilized upon variation of relative strength of direct versus indirect hopping and SOC, which differ in their Fermi surface topology. Fermi surfaces with different topology are found to be connected through intervening Lifshitz phase transitions. Remarkably, though, the ideal SU(8) point serves as a useful starting point to understand the global structure of the above phase diagram. In particular, the compensated metallic phases are found to be asymptotically connected to topological insulating states resulting from gapping out of SU(8) semimetals. Placing of the compounds, in the emergent $(t_{dd\sigma}/t_{ddm})$ - λ phase diagram, reveals the chloride compounds are close to the phase boundary separating two metals with different Fermi surface topology. Introduction of biaxial strain in these layered compounds is found to cause a large variation in the $t_{dd\sigma}/t_{ddm}$, and thereby could be an effective tool to induce Lifshitz transition in chloride compounds, in particular.

While the above study captures the physics of noninteracting electrons in the undimerized lattice, several possible ordering instabilities can be triggered in these compensated metallic phases at lower temperatures, as discussed in the following. For instance, electron-electron-interaction-driven ordering instabilities are expected to be particularly enhanced near the Lifshitz transitions [48,51,52] due to the

singular nature of single-particle density of states. Akin to the neck-collapsing Lifshitz transition and associated singular nature of the density of states found in the present case, similar phenomena have been discussed in Sr_2RuO_4 , which reports enhancement of instability near the Lifshitz point [50]. The renormalization group calculations for the short-ranged four-fermion interactions near the neck collapsing between two particle-like Fermi pockets indicate an enhancement of the BCS superconducting instability [53,54]. In particular, the neck-collapsing transition at the BZ boundary at M points between $F4$ and $F5$ opens up the possibility of finite momentum instabilities in both the particle-hole and particle-particle channels. The former can lead to a charge-density wave insulator generically accompanied by dimerization as observed in some of the candidate materials [34,55]. The finite momentum pairing instability leading to a Fulde-Ferrell-Larkin-Ovchinnikov (FFLO)-like [56,57] phase is equally interesting. These issues call for further detailed investigation.

Furthermore, the effect of short-ranged Hubbard interaction U , supplemented with a Hund scale J , relevant for multiorbital systems, energetically favors, within our GGA + U + SOC calculations (see Appendix F), a ferromagnetic metal in all the materials for lower values of $U - J$, which in turns gives way to ferromagnetic insulator and/or stripy and zigzag spin density wave insulators for larger $U - J$ values. We note that while we considered the magnetic and electronic properties over a broad range of $U - J$ values, the typical U value for early transition-metal compounds, especially for $4d$ and $5d$ series like Zr and Hf, is expected to be 1–2 eV [58]. The topology of the Fermi surface upon inclusion of correlation with choice of $U - J$, ~ 1 eV, remains unchanged as has been explicitly checked. This is, however, true for cases where the correlation-induced magnetic instability does not break the real-space symmetry of the lattice. The situation for Ti compounds, however, is less clear, which may actually show a metallic-to-insulator transition upon inclusion of $U - J$.

We further note the metallic state with net moment and topological character should lead to intrinsic anomalous Hall conductivity.

Finally, while the present study focuses on d^1 honeycomb compounds, it is straightforward to extend these ideas to materials with d^3 configuration such as MoCl_3 . Our minimal tight-binding model suggests a similarly rich fermiology in such materials including a curious exchange of flat band along the $\tau_m = 0$ line in Fig. 6. This will be taken up in the future.

ACKNOWLEDGMENTS

The authors acknowledge discussion with Arun Paramakanti, H. R. Krishnamurthy, and Vijay Shenoy. The authors acknowledge DST, Government of India (Nano mission), for funding under Project No. DST/NM/TUE/QM-10/2019 (C)/7. M.G. acknowledges CSIR, India, for the senior research fellowship [Grant No. 09/575 (0131) 2020-EMR-II]. B.M. and S.B. acknowledge the Max Planck Partner group grant at ICTS, Swarna Jayanti fellowship grant of SERB-DST (India) Grant No. SB/SJF/2021-22/12, and the Department of Atomic Energy, Government of India, under Project No. RTI4001. S.B. acknowledges the adjunct fellow program at SNBNCBS, Kolkata, for hospitality. T.S.D.

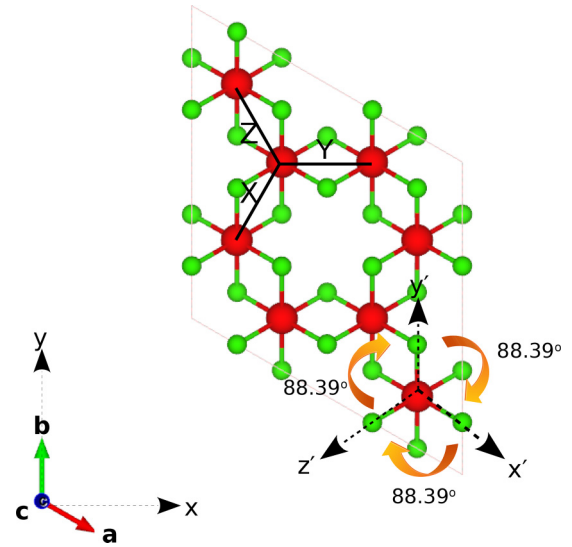


FIG. 12. Global and local coordinate systems denoted by x, y, z , and x', y', z' , respectively. Red and green balls represent metal (M) and halide (X) ions, respectively. A metal ion is connected to its nearest neighbors via X, Y , and Z bonds, also marked in the figure.

acknowledges a JC Bose National Fellowship (Grant No. JCB/2020/000004) for funding.

APPENDIX A: NUMERICAL DETAILS FOR OBTAINING THE PHASE DIAGRAM

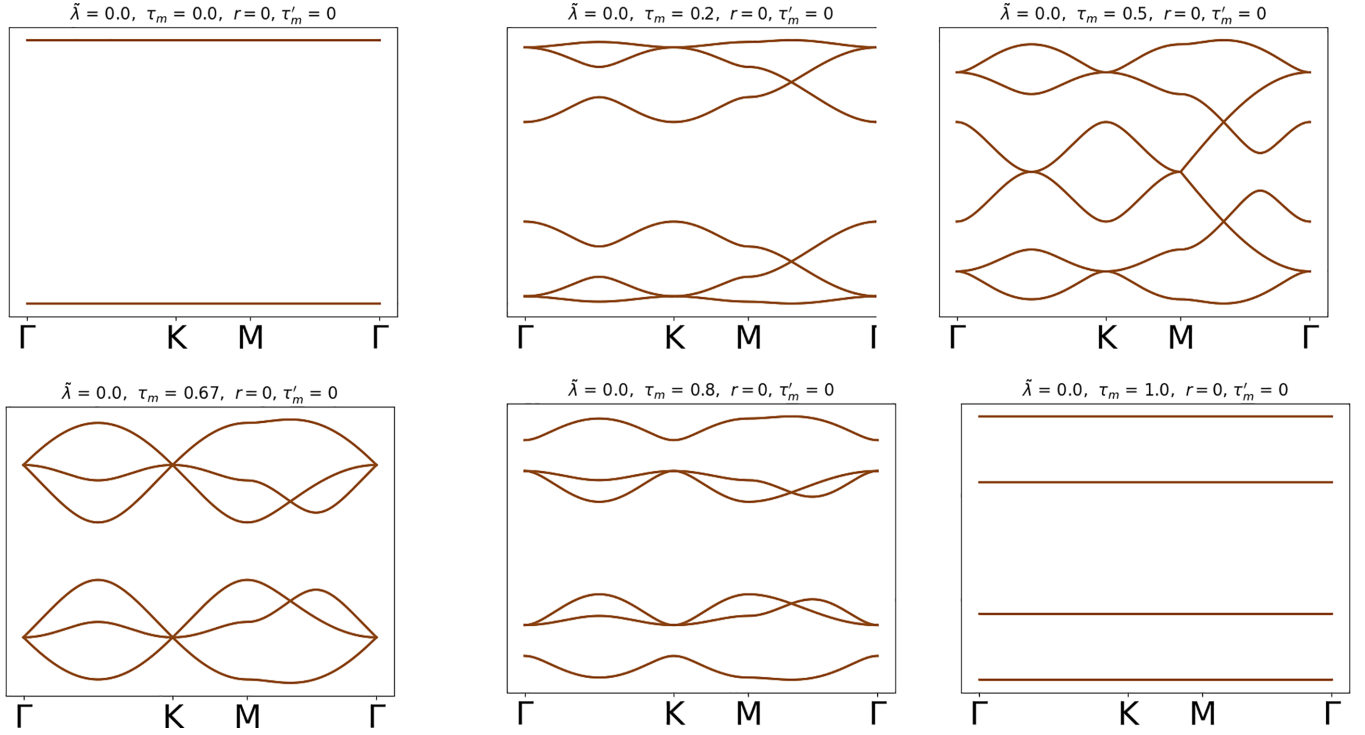
To draw the phase diagrams, we make a grid in the τ_m - $\tilde{\lambda}$ plane with the grid separation along both the τ_m and $\tilde{\lambda}$ axes being 10^{-2} . We determine the band structure at each grid point for the case of $1/6$ filling. For band insulators, we determine the topological Z_2 index of the filled band(s) using methods similar to Ref. [47]. We also plot the band structure with open boundary condition to check the presence of edge modes in case the Z_2 index is nontrivial (not shown). For band metals, we determine the shape of the corresponding Fermi surface by filling up the lowest energy states. The shapes of the different Fermi surfaces are differentiated based on three aspects: (a) the number of Fermi pockets, i.e., the number of different connected components, (b) whether the Fermi pockets are electron-like or hole-like, and (c) the point in the BZ around which the Fermi pockets appear.

APPENDIX B: TRANSFORMATION OF BASIS: GLOBAL TO HALIDE-BASED, PRIMED COORDINATE SYSTEM

In the global coordinate system, the x axis points in the direction making 30° with \mathbf{a} , y pointing along \mathbf{b} , and z along \mathbf{c} . A local octahedral coordinate system is defined by $x', y',$ and z' axes, where the corresponding x axis, y axis, and z axis point along the bonds $M-X$ as shown in Fig. 12.

The transformation matrix rotating the global coordinate system to the local coordinate system, for ZrCl_3 , is given by

$$\begin{aligned} x' &= (-0.7089)x + (0.4051)y + (-0.5772)z, \\ y' &= (0.0034)x + (-0.8165)y + (-0.5772)z, \\ z' &= (-0.7052)x + (-0.4112)y + (0.5774)z. \end{aligned}$$


 FIG. 13. Evolution of band structure along the $\tilde{\lambda} = 0$ line of the phase diagram in Fig. 6 of the main text.

It is to be noted that, due to trigonal distortion, the M-X bonds are not orthogonal to each other in the octahedron but have a mutual angle of 88.39° . Thus the above transformation matrix aligns the x' , y' , and z' axes, approximately, along the M-X bonds shown in Fig. 12. The rotation of the coordinate system, given above, gets reflected on d orbitals via the transformation matrix as

$$\begin{aligned}
 d_{x'y'} &= (0.5802)d_{xy} + (0.2374)d_{yz} + (0.5772)d_{z2} \\
 &\quad + (0.4072)d_{xz} + (0.3283)d_{x2-y2}, \\
 d_{y'z'} &= (0.5744)d_{xy} + (-0.2340)d_{yz} + (-0.5774)d_{z2} \\
 &\quad + (0.4091)d_{xz} + (-0.3382)d_{x2-y2}, \\
 d_{z'2} &= (0.5023)d_{xy} + (-0.4113)d_{yz} + (0.0001)d_{z2} \\
 &\quad + (-0.7053)d_{xz} + (0.2842)d_{x2-y2}, \\
 d_{x'z'} &= (0.0058)d_{xy} + (0.4713)d_{yz} + (-0.5774)d_{z2} \\
 &\quad + (-0.0022)d_{xz} + (0.6666)d_{x2-y2}, \\
 d_{x'2-y'2} &= (-0.2843)d_{xy} + (-0.7052)d_{yz} + (-0.0000)d_{z2} \\
 &\quad + (0.4112)d_{xz} + (0.5025)d_{x2-y2}.
 \end{aligned}$$

APPENDIX C: DERIVATION OF h_X, h_Y FROM h_Z

Since the Hamiltonian, given in Eq. (1) of the main text, is symmetric under the action of C_3 rotation, the hopping matrices on the Y and the X M-M bonds can be obtained from that on the Z bonds, by the transformation

$$h_X = \mathcal{R}_3^\dagger h_Z \mathcal{R}_3, \quad (\text{C1})$$

$$h_Y = \mathcal{R}_3^\dagger h_X \mathcal{R}_3. \quad (\text{C2})$$

Here, \mathcal{R}_3 is a 3×3 unitary operator that implements C_3 rotation about an axis perpendicular to the plane of the honeycomb lattice on the t_{2g} orbitals and is given by

$$\mathcal{R}_3 = \begin{pmatrix} 0 & 1 & 0 \\ 0 & 0 & 1 \\ 1 & 0 & 0 \end{pmatrix}. \quad (\text{C3})$$

APPENDIX D: EVOLUTION OF THE BAND STRUCTURES IN THE τ_m - $\tilde{\lambda}$ PHASE DIAGRAM

1. The $\tilde{\lambda} = 0$ line

Figure 13 shows the band structures at different points on the $\tilde{\lambda} = 0$ line of the τ_m - $\tilde{\lambda}$ phase diagram in Fig. 6(a) of the main text. At $\tau_m = 0$ on this line, there are two flat bands, each of which are sixfold degenerate. As τ_m is increased, six twofold-degenerate bands appear. Finally at $\tau_m = 1$, there are four bands with the lowest and the top bands being twofold and the rest being fourfold degenerate.

2. The $\tau_m = 0$ line

The energy spectrum along the $\tau_m = 0$ line is shown in Fig. 14. The band structure for $\tilde{\lambda} = 0$ (cf. the $\tilde{\lambda} = 0, \tau_m = 0$ line in Fig. 13) has two sixfold-degenerate bands. As $\tilde{\lambda}$ is increased, six twofold-degenerate bands appear, two of them being completely flat.

3. The $\tau_m = 1$ line

The evolution of the energy spectrum along the $\tau_m = 1$ line is shown in Fig. 15. The band structure for $\tilde{\lambda} = 0$ on this line has four bands (cf. $\tilde{\lambda} = 0, \tau_m = 1$ in Fig. 13). For large values

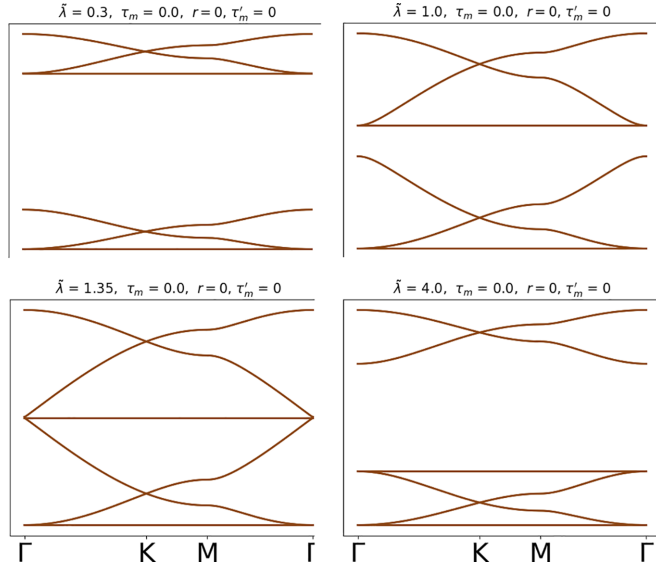


FIG. 14. Evolution of band structure along the $\tau_m = 0$ line of the phase diagram in Fig. 6 of the main text.

of $\tilde{\lambda}$, the $J = 3/2$ and the $J = 1/2$ bands are separated. For $\tilde{\lambda} = 20$, $\tau_m = 1$, only the lowest $J = 3/2$ bands are shown.

APPENDIX E: PROPERTIES OF GAPPED PHASES

1. SU(8) Dirac theory at the P_3 point

At the P_3 point of the phase diagram in Figs. 6 and 11 of the main text, the low-energy effective theory is described by massless Dirac fermions with internal SU(8) symmetry. Below we sketch the derivation of the Dirac theory. The details can be found in Ref. [19].

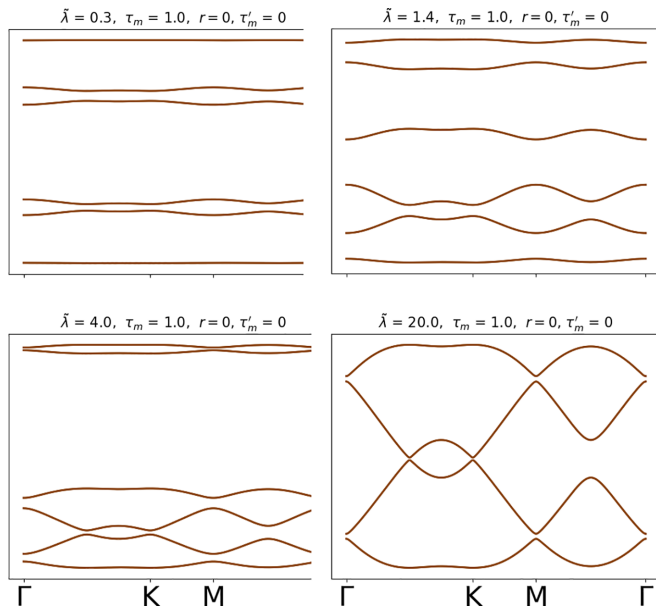


FIG. 15. Band structures along the $\tau_m = 1$ line of the phase diagram in Fig. 6 of the main text. All the bands are twofold degenerate. For $\tilde{\lambda} = 20$, only four bands are shown, leaving out higher energy $J = 1/2$ orbitals.

At the P_3 point, the form of the Hamiltonian in Eq. (5) of the main text, when projected to the low-energy $J = 3/2$ orbitals, is given by

$$\mathcal{H}_{P_3} = -\frac{\mathcal{E}}{\sqrt{3}} \left(\sum_{(ij) \in X\text{-bonds}} \psi_i^\dagger U_X \psi_j + \sum_{(ij) \in Y\text{-bonds}} \psi_i^\dagger U_Y \psi_j + \sum_{(ij) \in Z\text{-bonds}} \psi_i^\dagger U_Z \psi_j \right). \quad (\text{E1})$$

Here, ψ_i is a four-component annihilation operator corresponding to the four $J = 3/2$ orbitals at site i . The U_X , U_Y , and U_Z are 4×4 Hermitian matrices, which are given by

$$U_X = -\rho \Sigma_1, \quad (\text{E2})$$

$$U_Y = -\rho \Sigma_2, \quad (\text{E3})$$

$$U_Z = -\rho \Sigma_3. \quad (\text{E4})$$

Here, $\rho = +1$ for the phase diagram in Fig. 6(a) and $\rho = -1$ for Fig. 11. The Σ_i (for $i = 1, \dots, 15$) are the 15 linearly independent 4×4 traceless Hermitian matrices which are given in Appendix C of Ref. [19], which are essentially the generators of an SU(4) group. Note, the Hamiltonian in Eq. (E1) has an internal SU(4) symmetry [18].

Projecting this Hamiltonian in Eq. (E1) to the two lowest two bands which touch linearly at the Fermi energy, we get the SU(8) symmetric Dirac Hamiltonian given by

$$\mathcal{H}_{\text{Dirac}} = \rho v_F \int d^2 \mathbf{r} \chi^\dagger(\mathbf{r}) (-i\alpha_1 \partial_1 - i\alpha_2 \partial_2) \chi(\mathbf{r}), \quad (\text{E5})$$

with

$$\alpha_1 = \Sigma_0 \otimes \tau_3 \otimes \sigma_1, \quad (\text{E6})$$

$$\alpha_2 = \Sigma_0 \otimes \tau_0 \otimes \sigma_2. \quad (\text{E7})$$

Here, v_F is the Fermi velocity, which is related to the gradient of the linearly dispersing bands at the Dirac points. $\chi(\mathbf{r})$ is the 16-component Dirac spinor at the position \mathbf{r} . Both τ_i and σ_i (for $i = 1, 2, 3$) are the Pauli matrices with τ_0 and σ_0 being the 2×2 identity matrix. The generators of the SU(8) symmetry are the set of 63 matrices given by

$$\{\Sigma_0, \Sigma_i\} \otimes \{\tau_3 \sigma_0, \tau_1 \sigma_2, \tau_2 \sigma_2\}, \quad \Sigma_i \otimes \tau_0 \sigma_0, \quad (\text{E8})$$

for $i = 1, \dots, 15$.

2. The topological gapped phase

On moving left from the P_3 point along the $\tilde{\lambda} = \infty$ line by reducing the value of τ_m from 1, the effective hopping Hamiltonian in the $J = 3/2$ sector is given by

$$\mathcal{H}_{\text{top}} = -\frac{\mathcal{E}}{\sqrt{3}} \sum_{(ij)} \psi_i^\dagger \tilde{H}_{ij} \psi_j, \quad (\text{E9})$$

with

$$\begin{aligned}\tilde{H}_X &= U_X + (1 - \tau_m) \left[\frac{1}{3} \Sigma_0 + \frac{1}{6} (-\sqrt{3} \Sigma_4 + \Sigma_5) \right], \\ \tilde{H}_Y &= U_Y + (1 - \tau_m) \left[\frac{1}{3} \Sigma_0 + \frac{1}{6} (\sqrt{3} \Sigma_4 + \Sigma_5) \right], \\ \tilde{H}_Z &= U_Z + (1 - \tau_m) \left[\frac{1}{3} \Sigma_0 - \frac{1}{3} \Sigma_5 \right].\end{aligned}\quad (\text{E10})$$

On projecting this Hamiltonian to the lowest two bands, we get the following effective low-energy Hamiltonian:

$$\mathcal{H}_{\text{top}} = \mathcal{H}_{\text{Dirac}} + (1 - \tau_m) \mathcal{H}_m^{(1)} + (1 - \tau_m) \mathcal{H}'. \quad (\text{E11})$$

Here, $\mathcal{H}_{\text{Dirac}}$ is given by Eq. (E5). The $\mathcal{H}_m^{(1)}$ and \mathcal{H}' are given by

$$\mathcal{H}_m^{(1)} = \int d^2\mathbf{r} \chi^\dagger (\Sigma_1 \tau_1 \sigma_0 - \Sigma_2 \tau_2 \sigma_1 + \Sigma_3 \tau_0 \sigma_3) \chi \quad (\text{E12})$$

and

$$\mathcal{H}' = \chi^\dagger (-i\partial_x \delta\alpha_x - i\partial_y \delta\alpha_y) \chi, \quad (\text{E13})$$

with

$$\delta\alpha_x = -\Sigma_3 \tau_3 \sigma_1 + \frac{1}{\sqrt{3}} \Sigma_{35} \tau_0 \sigma_0 + \frac{\sqrt{3}}{2} \Sigma_{35} \tau_0 \sigma_3 \quad (\text{E14})$$

and

$$\begin{aligned}\delta\alpha_y &= \frac{1}{\sqrt{6}} (\Sigma_1 \tau_1 \sigma_2 - \Sigma_2 \tau_2 \sigma_2) \\ &+ \frac{\sqrt{3}}{2\sqrt{2}} (\Sigma_{14} \tau_1 \sigma_1 - \Sigma_{24} \tau_2 \sigma_1) \\ &- \frac{1}{2} (\Sigma_{14} \tau_2 \sigma_3 - \Sigma_{24} \tau_1 \sigma_3) \\ &- \frac{1}{2\sqrt{2}} (\Sigma_{15} \tau_1 \sigma_1 + \Sigma_{25} \tau_2 \sigma_1) \\ &+ \frac{1}{2\sqrt{3}} (\Sigma_{15} \tau_2 \sigma_3 + \Sigma_{25} \tau_1 \sigma_3).\end{aligned}\quad (\text{E15})$$

The term $\mathcal{H}_m^{(1)}$ is the ferroquadrupolar quantum Hall mass listed in Ref. [19] whose edge modes are protected by time-reversal (TR) symmetry. Thus, the phase obtained by moving left from the P_3 point in the phase diagram in Fig. 6(a) is a Z_2 topological insulator. The presence of \mathcal{H}' does not change the topological character of this phase since this term does not break the TR symmetry and can be tuned to zero without closing the fermionic energy gap.

3. The nontopological phase

On moving down vertically from the P_3 point along the $\tau_m = 1$ line, we encounter the nontopological gapped phase. This can be understood by doing a similar analysis as done for the previous gapped phase. For very large values of $\tilde{\lambda}$ and $\tau_m = 1$, the effective Hamiltonian is given by

$$\mathcal{H}_{\text{nontop}} = -\mathcal{E} \left(\sum_{\langle ij \rangle} \psi_i^\dagger U_{ij} \psi_j + \frac{1}{\tilde{\lambda}} \sum_{\langle\langle ij \rangle\rangle} \psi_i^\dagger \tilde{H}_{ij} \psi_j + \text{H.c.} \right), \quad (\text{E16})$$

where the U_{ij} are the matrices defined in Eq. (E2) and \tilde{H}_{ij} are the hopping matrices on the next-nearest-neighbor (NNN)

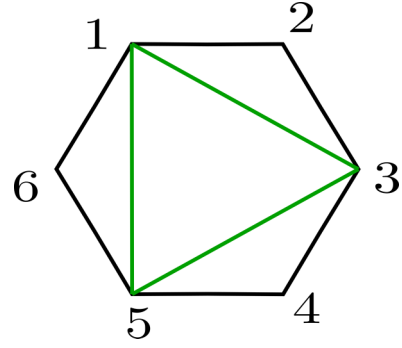


FIG. 16. A single hexagon of a honeycomb lattice showing the three kinds of next-nearest-neighbor bonds (green bonds). The six sites are labeled with integers from 1 to 6.

bonds of the lattice. On the three kinds of NNN bonds shown in Fig. 16, the \tilde{H}_{ij} matrices are given by

$$\begin{aligned}\tilde{H}_{13} &= -\frac{1}{2\sqrt{3}} \Sigma_1 + \frac{i}{6} (-\Sigma_{14} - \sqrt{3} \Sigma_{15} - \Sigma_{23}), \\ \tilde{H}_{35} &= -\frac{1}{2\sqrt{3}} \Sigma_2 + \frac{i}{6} (\Sigma_{13} - \Sigma_{24} + \sqrt{3} \Sigma_{25}), \\ \tilde{H}_{51} &= -\frac{1}{2\sqrt{3}} \Sigma_3 + \frac{i}{6} (-\Sigma_{12} + 2\Sigma_{34}).\end{aligned}\quad (\text{E17})$$

On projecting this Hamiltonian to the lowest two bands near the Dirac points, we get the following low-energy theory:

$$\mathcal{H}_{\text{nontop}} = \mathcal{H}_{\text{Dirac}} + \frac{1}{\lambda} \mathcal{H}_m^{(2)} + \frac{1}{\lambda} \mathcal{H}''. \quad (\text{E18})$$

Here, $\mathcal{H}_{\text{Dirac}}$ is the SU(8) symmetric Dirac Hamiltonian. The $\mathcal{H}_m^{(2)}$ is given by

$$\mathcal{H}_m^{(2)} = \int d^2x \chi^\dagger \Sigma_{45} \tau_3 \sigma_3 \chi. \quad (\text{E19})$$

The $\mathcal{H}_m^{(2)}$ is one of the topological masses proximate to the SU(8) Dirac semimetal. The edge modes of this topological symmetry are protected by a U(1) symmetry which is generated by Σ_{45} . But the term \mathcal{H}'' breaks this U(1) symmetry and destroys the edge modes. This explains the existence of the nontopological phase in the phase diagram.

4. Phase transition lines in τ_m - $\tilde{\lambda}$ plane with $\rho = \pm 1$

On the phase transition line, the $P_1 P_3$ line, between the two gapped phases shown in Fig. 6(a) of the main text, the lowest two bands touch each other linearly at the Γ point as shown in inset VI of the same figure. One can find the low-energy theory for this point of the phase diagram by projecting the Hamiltonian to the two lowest bands that touch at the Γ point. The resultant theory is given by

$$\mathcal{H}_\Gamma = -iv_F \int d^2x \chi_\Gamma^\dagger (\tau_3 \sigma_1 \partial_1 + \tau_0 \sigma_2 \partial_2) \chi_\Gamma. \quad (\text{E20})$$

Here, χ_Γ is a four-component spinor which comes from the twofold-degenerate Dirac cone at the Γ point. This Hamiltonian has an emergent SU(2) symmetry which is generated by $\{\tau_3 \sigma_0, \tau_1 \sigma_2, \tau_2 \sigma_2\}/2$.

TABLE III. Orbital and spin magnetic moments on metal (M) site for MX_3 , as calculated within GGA + U + SOC. $U - J$ value was chosen to be 3 eV for Ti and 2 eV for Zr and Hf.

MX_3	Orbital moment (μ_B)	Spin moment (μ_B)
TiF ₃	-0.061	0.922
TiCl ₃	-0.003	0.938
TiBr ₃	-0.008	0.965
ZrF ₃	-0.044	0.722
ZrCl ₃	-0.034	0.661
ZrBr ₃	-0.026	0.674
HfF ₃	-0.132	0.806
HfCl ₃	-0.104	0.626
HfBr ₃	-0.111	0.728

Similarly, on the P_3P_{14} line of the phase of Fig. 11, the lower two bands touch each other linearly at the three M points. The low-energy theory at any point on this line is given by

$$\mathcal{H}_M = i \int d^2x \chi_M^\dagger v_x \mathbb{I}_{3 \times 3} \otimes \tau_3 \sigma_1 \partial_1 + v_y \mathbb{I}_{3 \times 3} \otimes \tau_0 \sigma_2 \partial_2 \chi_M.$$

Here, χ_M is a 12-component spinor that comes from the three twofold-degenerate Dirac cones at the three M points. v_x and v_y are the Fermi velocities along the two Cartesian directions. The values of these two numbers depend on the position on the phase transition line. $\mathbb{I}_{3 \times 3}$ is the three-dimensional identity matrix that acts on the space of the three M valleys. This Hamiltonian has an internal SU(6) symmetry which is generated by the set of Hermitian matrices given by

$$\{\mathbb{I}_{3 \times 3}, \Lambda_i\} \otimes \{\tau_3 \sigma_0, \tau_1 \sigma_2, \tau_2 \sigma_2\}, \quad \Lambda_i \otimes \tau_0 \sigma_0, \quad (E21)$$

where the Λ_i are the eight 3×3 Gell-Mann matrices that generate an SU(3).

APPENDIX F: DFT COMPUTED MAGNETIC GROUND STATES

As discussed in main text, one of the possible consequences of inclusion of Coulomb correlation is to stabilize magnetism. To identify the magnetic ground states of the undimerized MX_3 compounds, DFT total energies for magnetic configurations, e.g., nonmagnetic (NM), ferromagnetic (FM), Néel antiferromagnetic (AFM), zigzag AFM (ZAFM), and stripe AFM (SAFM), were calculated within the GGA + U + SOC formulation to take into account of the Coulomb correlation in a mean-field way along with SOC, and compared. The Coulomb correlation is modeled through supplemented Hubbard U correction and the Hund coupling J to account for the multiorbital nature of the problem.

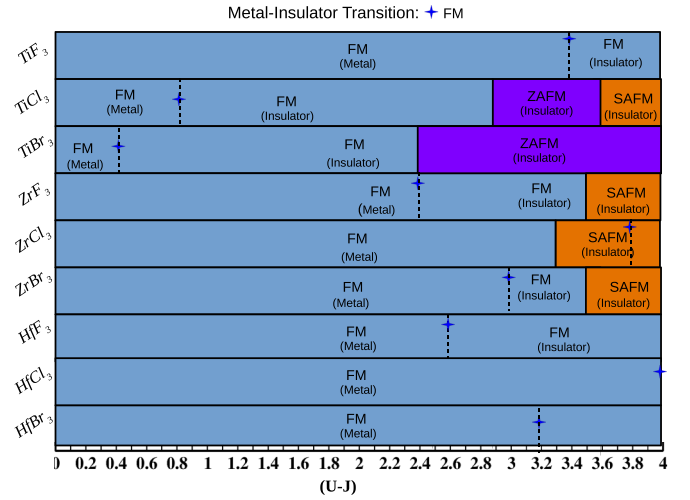


FIG. 17. Magnetic ground states for MX_3 for various different choices of $U - J$ (in eV).

The calculated spin and orbital magnetic moments of the nine compounds are tabulated in Table III. As expected, the orbital moment shows an increasing trend in moving from Ti to Zr to Hf compounds, while the spin moment shows a decreasing trend. This is justified by increase of SOC in moving from $3d$ to $4d$ to $5d$ in the transition-metal series, and the extended nature of the wavefunction in moving from $3d$ to $4d$ and $5d$.

The computed magnetic phase diagram is shown in Fig. 17 in the plane of compounds versus choice of $U - J$ parameter. Marked are the lowest-energy magnetic states according to DFT total energy, their conducting properties estimated from density of states plots. The metal-insulator transitions as well as magnetic transitions are marked by boundaries.

First of all, we notice in a large part of the phase diagram that the FM state is stabilized, with the exception of SAFM or ZAFM phases at large value of $U - J$ for Ti and Zr compounds. Although the $U - J$ is varied over a large range in the plot, the realistic estimates of U value for early transition metals like $3d$ Ti will be 3–4 eV, while that for $4d$ and $5d$ Zr and Hf will be 1–2 eV. With estimated J value of 1 eV for $3d$ transition metals and 0.4 eV for $4d$ and $5d$ transition metals, this amounts to a $U - J$ value of 2–3 eV for Ti compounds, and 0.6–1.6 eV for Zr and Hf compounds. With this choice, undimerized TiF₃ turns out to be FM metal, while TiCl₃ and TiBr₃ may exhibit stabilization of a ZAFM phase. For $4d$ and $5d$ Zr and Hf compounds, in undimerized structure, the FM metallic phase wins over the AFM phases.

- [1] G. Cao and L. E. Delong, *Frontiers of 4d- and 5d-Transition Metal Oxides* (World Scientific, Singapore, 2013).
 [2] W. Witczak-Krempa, G. Chen, Y. B. Kim, and L. Balents, Correlated quantum phenomena in the strong spin-orbit regime, *Annu. Rev. Condens. Matter Phys.* **5**, 57 (2014).

- [3] T. Takayama, J. Chaloupka, A. Smerald, G. Khaliullin, and H. Takagi, Spin-orbit-entangled electronic phases in 4d and 5d transition-metal compounds, *J. Phys. Soc. Jpn.* **90**, 062001 (2021).
 [4] X. Wan, A. M. Turner, A. Vishwanath, and S. Y. Savrasov, Topological semimetal and Fermi-arc surface states in the

- electronic structure of pyrochlore iridates, *Phys. Rev. B* **83**, 205101 (2011).
- [5] M. Z. Hasan and C. L. Kane, Colloquium: Topological insulators, *Rev. Mod. Phys.* **82**, 3045 (2010).
- [6] X.-L. Qi and S.-C. Zhang, Topological insulators and superconductors, *Rev. Mod. Phys.* **83**, 1057 (2011).
- [7] Y. Chen, J. G. Analytis, J.-H. Chu, Z. Liu, S.-K. Mo, X.-L. Qi, H. Zhang, D. Lu, X. Dai, Z. Fang *et al.*, Experimental realization of a three-dimensional topological insulator, Bi₂Te₃, *Science* **325**, 178 (2009).
- [8] J. Romhányi, L. Balents, and G. Jackeli, Spin-orbit dimers and noncollinear phases in d^1 cubic double perovskites, *Phys. Rev. Lett.* **118**, 217202 (2017).
- [9] G. Jackeli and G. Khaliullin, Mott insulators in the strong spin-orbit coupling limit: From Heisenberg to a quantum compass and Kitaev models, *Phys. Rev. Lett.* **102**, 017205 (2009).
- [10] G. Chen, R. Pereira, and L. Balents, Exotic phases induced by strong spin-orbit coupling in ordered double perovskites, *Phys. Rev. B* **82**, 174440 (2010).
- [11] C. Broholm, R. Cava, S. Kivelson, D. Nocera, M. Norman, and T. Senthil, Quantum spin liquids, *Science* **367**, eaay0668 (2020).
- [12] J. Knolle and R. Moessner, A field guide to spin liquids, *Annu. Rev. Condens. Matter Phys.* **10**, 451 (2019).
- [13] H. Takagi, T. Takayama, G. Jackeli, G. Khaliullin, and S. E. Nagler, Concept and realization of Kitaev quantum spin liquids, *Nat. Rev. Phys.* **1**, 264 (2019).
- [14] B. J. Kim, H. Jin, S. J. Moon, J.-Y. Kim, B.-G. Park, C. S. Leem, J. Yu, T. W. Noh, C. Kim, S.-J. Oh, J.-H. Park, V. Durairaj, G. Cao, and E. Rotenberg, Novel $J_{\text{eff}} = 1/2$ Mott state induced by relativistic spin-orbit coupling in Sr₂IrO₄, *Phys. Rev. Lett.* **101**, 076402 (2008).
- [15] B. Kim, H. Ohsumi, T. Komesu, S. Sakai, T. Morita, H. Takagi, and T.-h. Arima, Phase-sensitive observation of a spin-orbital Mott state in Sr₂IrO₄, *Science* **323**, 1329 (2009).
- [16] J. Kim, D. Casa, M. H. Upton, T. Gog, Y.-J. Kim, J. F. Mitchell, M. Van Veenendaal, M. Daghofer, J. van den Brink, G. Khaliullin, and B. J. Kim, Magnetic excitation spectra of Sr₂IrO₄ probed by resonant inelastic x-ray scattering: Establishing links to cuprate superconductors, *Phys. Rev. Lett.* **108**, 177003 (2012).
- [17] M. A. McGuire, Crystal and magnetic structures in layered, transition metal dihalides and trihalides, *Crystals* **7**, 121 (2017).
- [18] M. G. Yamada, M. Oshikawa, and G. Jackeli, Emergent SU(4) symmetry in α -ZrCl₃ and crystalline spin-orbital liquids, *Phys. Rev. Lett.* **121**, 097201 (2018).
- [19] B. Mondal, V. B. Shenoy, and S. Bhattacharjee, Emergent SU(8) Dirac semimetal and novel proximate phases of spin-orbit coupled fermions on a honeycomb lattice, [arXiv:2304.07223](https://arxiv.org/abs/2304.07223) [Phys. Rev. B (to be published)].
- [20] J. Kanamori, Superexchange interaction and symmetry properties of electron orbitals, *J. Phys. Chem. Solids* **10**, 87 (1959).
- [21] C. L. Kane and E. J. Mele, Quantum spin Hall effect in graphene, *Phys. Rev. Lett.* **95**, 226801 (2005).
- [22] T. Senthil, Symmetry-protected topological phases of quantum matter, *Annu. Rev. Condens. Matter Phys.* **6**, 299 (2015).
- [23] P. E. Blöchl, Projector augmented-wave method, *Phys. Rev. B* **50**, 17953 (1994).
- [24] A. Tackett, N. Holzwarth, and G. Matthews, A projector augmented wave (PAW) code for electronic structure calculations, part II: PWPW for periodic solids in a plane wave basis, *Comput. Phys. Commun.* **135**, 348 (2001).
- [25] J. Paier, R. Hirschl, M. Marsman, and G. Kresse, The Perdew-Burke-Ernzerhof exchange-correlation functional applied to the G2-1 test set using a plane-wave basis set, *J. Chem. Phys.* **122**, 234102 (2005).
- [26] G. Kresse and J. Hafner, *Ab initio* molecular dynamics for liquid metals, *Phys. Rev. B* **47**, 558 (1993).
- [27] E. Eliav, U. Kaldor, and Y. Ishikawa, Open-shell relativistic coupled-cluster method with Dirac-Fock-Breit wave functions: Energies of the gold atom and its cation, *Phys. Rev. A* **49**, 1724 (1994).
- [28] G. Kresse and D. Joubert, From ultrasoft pseudopotentials to the projector augmented-wave method, *Phys. Rev. B* **59**, 1758 (1999).
- [29] J. P. Perdew, K. Burke, and M. Ernzerhof, Generalized gradient approximation made simple, *Phys. Rev. Lett.* **77**, 3865 (1996).
- [30] S. L. Dudarev, G. A. Botton, S. Y. Savrasov, C. J. Humphreys, and A. P. Sutton, Electron-energy-loss spectra and the structural stability of nickel oxide: An LSDA + U study, *Phys. Rev. B* **57**, 1505 (1998).
- [31] S. Grimme, Semiempirical GGA-type density functional constructed with a long-range dispersion correction, *J. Comput. Chem.* **27**, 1787 (2006).
- [32] O. K. Andersen and O. Jepsen, Explicit, first-principles tight-binding theory, *Phys. Rev. Lett.* **53**, 2571 (1984).
- [33] O. K. Andersen and T. Saha-Dasgupta, Muffin-tin orbitals of arbitrary order, *Phys. Rev. B* **62**, R16219 (2000).
- [34] S. I. Troyanov, E. M. Snigireva, and V. B. Rybakov, An x-ray structural investigation of the phase transition in α -TiCl₃, *Russ. J. Inorg. Chem.* **36**, 634 (1991).
- [35] G. Allegra, Il calcolo dell'intensità di diffrazione dei raggi X da parte di strutture denotanti disordine monodimensionale: Iii-studio strutturale di due diverse modificazioni cristalline del tiCl₃ che presentano disordine monodimensionale, *Il Nuovo Cimento (1955-1965)* **23**, 502 (1962).
- [36] The in-plane lattice constant of TiCl₃ in AAA, ABA, and ABC is found to vary from 6.14 to 6.153 Å, while the interlayer separation is found to vary from 5.850 to 5.866 Å.
- [37] T. R. Devidas, N. V. C. Shekar, C. S. Sundar, P. Chithaiah, Y. A. Sorb, V. S. Bhadram, N. Chandrabhas, K. Pal, U. V. Waghmare, and C. N. R. Rao, Pressure-induced structural changes and insulator-metal transition in layered bismuth triiodide, BiI₃: A combined experimental and theoretical study, *J. Phys.: Condens. Matter* **26**, 275502 (2014).
- [38] J. Ketelaar, C. MacGillavry, and P. Renes, The crystal structure of aluminium chloride, *Recl. Trav. Chim.* **66**, 501 (1947).
- [39] S. I. Troyanov, V. M. Ionov, and V. B. Rybakov, Synthesis and crystal structures of TiBr₄, TiBr₃, and Ti(AlBr₄)₂, *Zh. Neorg. Khim.* **35**, 882 (1990).
- [40] B. Swaroop and S. Flengas, Crystal structure of zirconium trichloride, *Can. J. Phys.* **42**, 1886 (1964).
- [41] J. Daintith, *A Dictionary of Chemistry* (Oxford University Press, Oxford, UK, 2008).
- [42] P. A. Maksimov, A. V. Ushakov, Z. V. Pchelkina, Y. Li, S. M. Winter, and S. V. Streltsov, *Ab initio* guided minimal model for the "Kitaev" material BaCo₂(AsO₄)₂: Importance of direct hopping, third-neighbor exchange, and quantum fluctuations, *Phys. Rev. B* **106**, 165131 (2022).

- [43] D. Guterding, H. O. Jeschke, and R. Valentí, Prospect of quantum anomalous Hall and quantum spin Hall effect in doped kagome lattice Mott insulators, *Sci. Rep.* **6**, 25988 (2016).
- [44] N. Goldman, D. F. Urban, and D. Bercioux, Topological phases for fermionic cold atoms on the Lieb lattice, *Phys. Rev. A* **83**, 063601 (2011).
- [45] I. Lifshitz *et al.*, Anomalies of electron characteristics of a metal in the high pressure region, *Sov. Phys. JETP* **11**, 1130 (1960).
- [46] G. Volovik, Topological Lifshitz transitions, *Low Temp. Phys.* **43**, 47 (2017).
- [47] L. Fu and C. L. Kane, Topological insulators with inversion symmetry, *Phys. Rev. B* **76**, 045302 (2007).
- [48] Y. Yamaji, T. Misawa, and M. Imada, Quantum and topological criticalities of Lifshitz transition in two-dimensional correlated electron systems, *J. Phys. Soc. Jpn.* **75**, 094719 (2006).
- [49] M. Rodney, H. F. Song, S.-S. Lee, K. Le Hur, and E. S. Sørensen, Scaling of entanglement entropy across Lifshitz transitions, *Phys. Rev. B* **87**, 115132 (2013).
- [50] V. Sunko, E. Abarca Morales, I. Marković, M. E. Barber, D. Milosavljević, F. Mazzola, D. A. Sokolov, N. Kikugawa, C. Cacho, P. Dudin *et al.*, Direct observation of a uniaxial stress-driven Lifshitz transition in Sr_2RuO_4 , *npj Quantum Mater.* **4**, 46 (2019).
- [51] H.-Y. Kee, E. H. Kim, and C.-H. Chung, Signatures of an electronic nematic phase at the isotropic-nematic phase transition, *Phys. Rev. B* **68**, 245109 (2003).
- [52] S. T. Carr, J. Quintanilla, and J. J. Betouras, Lifshitz transitions and crystallization of fully polarized dipolar fermions in an anisotropic two-dimensional lattice, *Phys. Rev. B* **82**, 045110 (2010).
- [53] S. Ghamari, S.-S. Lee, and C. Kallin, Renormalization group analysis of a neck-narrowing Lifshitz transition in the presence of weak short-range interactions in two dimensions, *Phys. Rev. B* **92**, 085112 (2015).
- [54] A. Kapustin, T. McKinney, and I. Z. Rothstein, Wilsonian effective field theory of two-dimensional Van Hove singularities, *Phys. Rev. B* **98**, 035122 (2018).
- [55] V. V. Gapontsev, D. D. Gazizova, and S. V. Streltsov, Dimerization in $\alpha\text{-TiCl}_3$ and $\alpha\text{-TiBr}_3$: The DFT study, *J. Phys.: Condens. Matter* **33**, 495803 (2021).
- [56] P. Fulde and R. A. Ferrell, Superconductivity in a strong spin-exchange field, *Phys. Rev.* **135**, A550 (1964).
- [57] A. I. Larkin and Y. N. Ovchinnikov, Nonuniform state of superconductors, *Zh. Eksp. Teor. Fiz.* **47**, 1136 (1964).
- [58] J. W. Bennett, B. G. Hudson, I. K. Metz, D. Liang, S. Spurgeon, Q. Cui, and S. E. Mason, A systematic determination of Hubbard U using the GBRV ultrasoft pseudopotential set, *Comput. Mater. Sci.* **170**, 109137 (2019).